Impact of a Strong Biomass Burning Event on the Radiative Forcing in the Arctic

Justyna Lisok[1], Anna Rozwadowska[2], Jesper G. Pedersen[1], Krzysztof M. Markowicz[1], Christoph Ritter[3], Jacek W. Kaminski[4], Joanna Struzewska[5], Mauro Mazzola[6], Roberto Udisti[6,7], Silvia Becagli[7], and Izabela Górecka[8]

[1]Institute of Geophysics, Faculty of Physics, University of Warsaw, Poland
[2]Institute of Oceanology, Polish Academy of Sciences, Sopot, Poland
[3]Alfred Wegener Institute for Polar and Marine Research, Potsdam, Germany
[4]Department of Atmospheric Physics, Institute of Geophysics, Polish Academy of Sciences, Warsaw, Poland
[5]Faculty of Building Services Hydro and Environmental Engineering, Warsaw University of Technology, Warsaw, Poland
[6]National Research Council, Institute of Atmospheric Sciences and Climate, Bologna, Italy
[7]Department of Chemistry, University of Florence, Florence, Italy
[8]Geoterra, Gdańsk, Poland

Correspondence to: Justyna Lisok (jlisok@igf.fuw.edu.pl)

Abstract. The aim of the presented study was to investigate the impact on the radiation budget of a biomass burning plume, transported from Alaska to a high Arctic region (Ny-Ålesund, Svalbard), in early July 2015. This large aerosol load event is considered exceptional in the last 25 years, with mean aerosol optical depth increased by the factor of 10, in comparison to the average summer background values. We utilised in situ data with hygroscopic growth equations, as well as remote sensing measurements as inputs to radiative transfer models, with an objective to estimate biases associated with (i) hygroscopicity, (ii) variability of single-scattering albedo profiles, and (iii) plane-parallel closure of the modeled atmosphere. A chemical weather model with satellite-derived biomass burning emissions was used to interpret the transport and transformations pathways.

Provided MODTRAN radiative transfer model simulations for the smoke event (14:00 July 9th - 11:30 July 11th) resulted in the mean aerosol direct radiative forcing on the level of -78.9 Wm^{-2} and -47.0 Wm^{-2}, at the surface and the top of the atmosphere respectively, for the mean value of aerosol optical depth equal to 0.64 at 550 nm. It corresponded to the average clear-sky direct radiative forcing of -43.3 Wm^{-2}, estimated by radiometer and model simulations at the surface. Ultimately, uncertainty connected with the plane-parallel atmosphere approximation altered results by about 2 Wm^{-2}. Furthermore, model-derived aerosol direct radiative forcing efficiency reached on average -126 $\mathrm{Wm}^{-2}/\tau_{550}$ and -71 $\mathrm{Wm}^{-2}/\tau_{550}$ at the surface and at the top of the atmosphere. Estimated heating rate up to 1.8 Kday^{-1} inside the BB plume, implied vertical mixing with turbulent kinetic energy of 0.3 $\mathrm{m}^2\mathrm{s}^{-2}$.

1 Introduction

Wildfires are considered significant sources of carbon in the atmosphere. It is estimated that up to 2.0 Pg of carbon aerosol is released into the atmosphere each year (Van der Werf et al., 2010). In the past 100 years, an intensification of fires in

mid-latitudes is observed appreciably affecting radiative and optical properties of the atmosphere (Mtetwa and McCormick, 2003). The emitted particles from biomass burning (BB) sources mainly consist of organic and black carbon (IPCC, 2001) of which 90% are built of the fine mode regarding aerosol size distribution (Dubovik et al., 2002). The impact of the plume on the atmospheric instability conditions and its rather small particle radius might result in a rapid transport on an intercontinental

5 scale, within just several days (Nikonovas et al., 2015). Thus, it is likely that the biomass burning aerosol considerably affects the optical and radiative properties of the atmosphere in the substantial part of the globe. The influence of BB aerosol is manifested by heating the air layer where transport takes place. Regarding the columnar properties however, it implies weak cooling effects at the top of the atmosphere (TOA) due to predominant scattering properties of the plume (Hansen et al., 2004). The magnitude of its impact is nevertheless strongly dependent on the chemical composition that results from the adversative

10 radiative response of the atmosphere exposed to black and organic carbon, being negative for the latter (Myhre et al., 2013a).

A number of papers analysed the associated annual mean value of instantaneous clear-sky aerosol direct radiative forcing (RF) at TOA (RF_{toa}). Myhre et al. (2013a) presented the results from AeroComII's 28 models, indicating a global mean BB RF_{toa} on the level of -0.01 ± 0.08 Wm^{-2}. This very similar value was presented by Myhre et al. (2013b) in the Fifth Assessment IPCC Report, being equal to 0.0 ± 0.2 Wm^{-2}. Despite a rather low (and negative) mean global value of BB RF_{toa}

15 on a regional scale (especially over bright surfaces), smoke may play a substantial role in affecting radiative properties of the atmosphere (Wang et al., 2006). In a high surface albedo case, the existence of smoke particles leads to albedo changes of the underlying clouds and the surface; and that in turn may indicate a positive RF_{toa} (Screen and Simmonds, 2010), leading to positive feedback within the entire atmospheric column. Therefore, the annual median value of ensemble RF_{toa} in the Arctic region, at the level of 0.01 Wm^{-2}, was reported by Sand et al. (2017) in light of AeroCom Phase II multi-model evaluations.

20 Similar results are presented in Wang et al. (2014), who estimated its value of around 0.004 Wm^{-2}.

The accurate parameterization of aerosol single-scattering properties as inputs to radiative transfer simulations at a regional scale, is of great concern in the Arctic region due to sparse spatial distribution of long-term, ground-based measurements (Markowicz et al., 2017a) and a high mean cloud fraction (especially in the summer), which restrains satellite retrievals. Therefore, it is unlikely to properly represent parameters associated with the highest RF uncertainties, such as changes in

25 the aerosol optical and microphysical properties undergoing ageing processes, while transported across a large region (Bond et al., 2013; Ortiz-Amezcua et al., 2017; Koch et al., 2009; Janicka et al., 2017). In single-cell simulations at a certain location, aerosol single-scattering properties might be investigated by inversion schemes utilising sun-photometer data that are retrieved under the AERONET network. However, the uncertainty of the columnar single-scattering albedo (ω) retrieval becomes high, considering low levels of aerosol optical depth (τ; Dubovik et al., 2000). This is the reason why AERONET level 2 data

30 validation is performed only for τ_{440} more than 0.5 and solar zenith angle above 50° (Dubovik et al., 2002). This, in turn, leads to a significant reduction of data coverage calculated for the Arctic region (Markowicz et al., 2017a).

The above aerosol properties may also be calculated utilising in situ measurements, however, taking into account the fact that they are carried out at a certain temperature (usually around 20-30°C) that causes water evaporation, and therefore a reduction of aerosol optical properties associated with their hygroscopic properties. The impact of water uptake by aerosol is significant,

35 regarding soluble particles when exposed to a relative humidity (RH) of more than 40%, resulting in the enhancement of a

particle scattering cross-section (Orr et al., 1958). Some studies apply empirical formulas of an enhancement factor $f(RH)$ to retrieve the aerosol optical properties at ambient conditions (Kotchenruther and Hobbs, 1998), defined as the ratio between particle radius at ambient conditions and at RH fixed to 30 %. The absolute values of growth factor may vary significantly due to the particle chemical composition related to the emission source (Gras et al., 1999; Magi et al., 2003; Kreidenweis et al.,
5   2001) and additionally, due to particle size (Carrico et al., 2010). Regarding fresh and aged plumes of biomass burning aerosol, $f(RH)$ were found to be 1.1 and 1.35 respectively at RH of around 80 %. This $f(RH)$ enhancement due to the ageing process is in agreement with secondary production of sulphate and progressive oxidation of organic compounds with OH and COOH groups, that result in increasing the hygroscopic properties (Reid et al., 2005).

Previously presented by scientific papers, and characterized in this research, was the study of smoke transport over the Arctic
10 during July 2015. Markowicz et al. (2016a) reported the temporal and spatial variability of aerosol single-scattering properties measured by in situ and ground-based remote sensing instruments over Svalbard and in Andenes, Norway. Moroni et al. (2017), discussed morphochemical characteristics and mixing state of smoke particles in Ny-Ålesund as indicated by DEKATI 12-stage low volume impactor, combined with scanning electron microscopy. Markowicz et al. (2017b) on the other hand, presented a comprehensive description of smoke radiative and optical properties on a regional scale. The paper examined ageing processes
15 of the smoke plume under study, while transported from the source region across the High Arctic. Simple Fu-Liou radiative transfer model, combined with NAAPS aerosol transport model, were used to determine the spatial distribution of aerosol single-scattering properties and RFs for the period of 5-15 July 2015, in the area to the north of 55°N, where the transport of BB aerosol was observed.

In this paper, we utilise MODTRAN radiative transfer simulations and aerosol optical properties obtained from in situ and
20 ground-based remote sensing instruments, to retrieve clear-sky direct RF over the area close to Ny-Ålesund. The research aims to estimate the biases connected with (i) hygroscopicity, (ii) variability of ω profiles, and (iii) plane-parallel closure of the modeled atmosphere. The main outcome of this research is the implementation of new methodology to retrieve the profile of ω at ambient conditions, utilising in situ measurements and lidar profiles (section 3.2). Simulated RFs were compared to simple radiative transfer model (section 3.5). Section 3.6 shows an example of RF distribution at the surface, in the vicinity
25 of Kongsfjorden. The last part presents the influence of unstably stratified biomass burning air masses on the turbulence development, which is shown in section 3.7. Additionally, we confirmed the source region of the BB plume. A chemical weather model with satellite-derived biomass burning emissions was used to interpret the transport and transformations pathways.

2   Methodology

This chapter consists of a few subsections dedicated to a brief description of all data and models used in this research. In
30 paragraph 2.1 we will focus on characterization of all models used to track the transport of smoke, as well as to calculate the impact of the BB plume on radiative and dynamical properties of the atmosphere.

2.1 Modeling tools

The MODerate-resolution atmospheric radiance and TRANsmittance model (MODTRAN) v. 5.2.1 (Berk et al., 1998) is the radiative transfer model (RTM). In this study, simulations are run with 17 defined absorption coefficients for each band in a correlated-k scheme (multiple scattering included; Bernstein et al., 1996), 8-stream discrete ordinate radiative transfer (DISORT) method, with a spectral resolution of 15 cm^{-1} of the radiation fluxes (Stamnes et al., 1988), as well as Henyey - Greenstein scattering phase function approximation (Henyey and Greenstein, 1941). Calculations are performed for the user-defined vertical profiles of thermodynamical variables, as well as aerosol and trace gases' optical properties, provided by HITRAN 2000 database (Rothman et al., 1998). MODTRAN was run with the time resolution of 20 min from 9th to 11th July 2015, for the domain set to Ny-Ålesund coordinates. Simulations included cases with and without aerosol load ('polluted' and 'reference').

The Fu-Liou v. 200503 (Fu and Liou, 1992, 1993) RTM uses the δ 2/4 stream solver, applied for 6 shortwave and 12 longwave spectral bands. The optical properties of the atmosphere are calculated by the correlated-k distribution method, defined for each spectral band (Fu and Liou, 1992). The optical properties of aerosols, as well as thermodynamical properties of the atmosphere, were based on the results provided by NAAPS (Navy Aerosol Analysis and Prediction System) global aerosol model re-analysis (Lynch et al., 2016).

3D effects of the RF were calculated using 3D forward Monte Carlo code (Marshak et al., 1995), which utilises a maximum cross-section method to compute photon paths in the three-dimensional model of the atmosphere (Marchuk et al., 2013). A number of modifications were made to the original setup of the code, including such phenomena as absorption of photons by atmospheric gases, reflection and absorption at the undulated Earth's surface (Rozwadowska and Górecka, 2012, 2017). The model domain covers the area of 51 km (W-E axis) x 68 km (S-N axis) and consists of cells/columns of 200 x 200 m. The main domain is surrounded by a 20 km wide belt, in order to reduce the impact of cyclic boundaries on the results in the Monte Carlo modeling. The computations were performed for the whole 91 x 108 km domain, but only the results from the main domain were analyzed. The Earth's surface was represented by the Digital Elevation Model (DEM), and the technique proposed by Ricchiazzi and Gautier (1998).

Implicit large-eddy simulations (ILESs) were performed using the 3D nonhydrostatic anelastic Eulerian-semi-Lagrangian (EULAG) model (Prusa et al., 2008), to estimate the dynamical response of the atmosphere induced by the BB plume. The EULAG model is set up to solve for the three velocity components u, v, and w in the x-, y-, and z-directions (i.e. W-E, S-N, and vertical directions), as well as the potential temperature (θ). The governing equations are solved in an Eulerian framework without explicit subgrid-scale (SGS) terms included. The nonoscillatory forward-in-time integration is performed with the Multidimensional Positive definite Advection Transport Algorithm (MPDATA; Smolarkiewicz, 2006). We rely on the ability of the MPDATA to implicitly account for the effect of unresolved turbulence on the resolved flow, through the truncation terms associated with the algorithm. For more details on ILES, see e.g. Grinstein et al. (2007). The horizontal grid spacing was set to 200 m and the vertical grid spacing to 50 m. The size of the computational domain was set to 19 km in the horizontal directions and 20 km in the vertical direction. The uppermost 5 km is a sponge layer included to prevent reflection of gravity waves at

the top of the domain. The upper boundary of the domain is impermeable with a free slip condition, and the lower boundary is impermeable with partial slip conditions, characterized by a specified drag coefficient of 0.001. The flow is periodic across the lateral boundaries of the domain. The EULAG simulations were calculated for 12:00 UTC, 10th July 2015, in Ny-Ålesund, using results obtained from the radiative transfer model and radio-sounding data.

5   Global Environmental Multiscale model with atmospheric chemistry (GEM-AQ; Côté et al., 1998; Kaminski et al., 2008), was run in a global configuration with a uniform grid resolution of 0.9^o. The vertical domain was defined on 28 hybrid levels with the model top at 10 hPa. Biomass burning emissions were taken from the Global Fire Assimilation System (GFAS; Kaiser et al., 2012). In addition to comprehensive tropospheric chemistry, the GEM-AQ model has 5 size-resolved aerosol species: sea salt, sulphate, black carbon, organic carbon, and dust. The microphysical processes that describe formation

10   and transformation of aerosols are calculated by a sectional aerosol module (Gong, 2003). The particle mass is distributed into 12 logarithmically spaced bins from 0.005 to 10.24 μm. The aerosol module accounts for: nucleation, condensation, coagulation, sedimentation and dry deposition, in-cloud oxidation of SO_2, in-cloud scavenging, and below-cloud scavenging by rain and snow. Calculations of τ are done on-line for all bins and aerosol species. Extinction cross-sections are taken from the AODSEM model (Aubé et al., 2000, 2004). The anthropogenic emissions, based on ECLIPSEv4 (http://www.iiasa.ac.at/

15   web/home/research/researchPrograms/air/ECLIPSEv4a.html), were used. The model was run for the period from 15 June to 20 July 2015.

2.2   Instruments

In this section, we present a brief description of all instruments located in Ny-Ålesund, used for this research study (Tab. 1). For a more detailed specification, one is encouraged to read a section concerning instrumentation in Markowicz et al. (2016a).

20   τ, Ångstrom exponent (α) and precipitable water (PW) were measured by Full-Automatic Sun Photometer SP1a (Dr. Schulz & Partner GmbH). The instrument obtains direct solar radiation in 10 channels ranging from 369 and 1023 nm with 1° field of view (Herber et al., 2002). Corrections included temperature variability, Langley methodology, and cloud-screening algorithms (Smirnov et al., 2000; Alexandrov et al., 2004).

     Extinction profiles were retrieved from KARL Raman lidar. The instrument uses Nd:Yag laser pulse at 355, 532, 1064

25   nm with the power of 10 W at each wavelength, to obtain backscatter and extinction coefficients. Also, the depolarization is measured at water vapour channels (407, 660 nm). The detection is carried out by 70 cm mirror with a 1.75 mrad field of view, and the overlap issue is fulfilled at 700 m a.g.l. Further details may be found in Hoffmann (2011) and Ritter et al. (2016).

     Continuous measurements of radiation fluxes are provided in Ny-Ålesund under the Baseline Surface Radiation Network (BSRN). Ball-shaded CMP22 by Kipp&Zonen installed on solar tracker by Schulz & Partner, measures total incoming and

30   reflected solar radiation at 200 - 3600 nm (Maturilli et al., 2015).

     The in situ measurements of single-scattering properties were provided in the Gruvebadet Laboratory, located 1 km south-west from Ny-Ålesund. Single wavelength M903 Nephelometer from Radiance Research, uses xenon flash lamp and opal diffuser to derive scattering coefficient at 530 nm (Müller et al., 2009) with an angular integration range of 10- 170°. Corrections for non-ideal illumination and truncation error were performed according to the description presented in Müller et al. (2009).

Table 1. Description of the instruments installed in Ny-Ålesund used as input data for atmospheric radiative transfer model.

Ground based Instrument	Wavelength, Size [nm]	Quantities*	Δ t [min]	Station
AWI Aerosol Raman lidar KARL	355, 387, 407, 532, 607, 660, 1064	σ_{ext}	30	village
AWI Sun photometer SP1a	369, 381, 413, 500, 610, 674, 779, 860, 945, 1023	τ, α, PW	1	village
Scanning Mobility Particle Sizer Spectrometer SMPS 3034	10-487	ASD	10	Gruvebadet laboratory
Aerodynamic Particle Sizer APS 3321	523-20 000	ASD	10	Gruvebadet laboratory
Particle Soot Absorption Photometer	467, 530, 660	σ_{abs}	60	Gruvebadet laboratory
Nephelometer M903	530	σ_{scat}	60	Gruvebadet laboratory
Pyranometer	200-3600	F_{in}, F_{out}	1	village

*σ_{ext} - extinction coefficient, τ- aerosol optical depth, α - Ångstrom exponent, PW - precipitable water, ASD - aerosol size distribution, σ_{abs} - absorption coefficient, σ_{scat} - scattering coefficient, F_{in} - total incoming flux, F_{out} - total outgoing flux bot at the surface

Black carbon (BC) concentration and aerosol absorption coefficient were measured at 467, 530, 660 nm by the Particle Soot Absorption Photometer (PSAP) from Radiance Research, based on the principle of filter attenuation change due to aerosol load. Corrections for multiple scattering and non-purely absorbing aerosols were done following methodology from Haywood and Osborne (2000).

5   Aerosol size distribution measurements were covered by joint spectra of TSI Scanning Mobility Particle Sizer (SMPS 3034), with 54 channels and TSI Aerodynamic Particle Sizer Spectrometer (APS 3321), with 52 channels. Jointly, the spectral coverage is in a range of 10-20 000 nm excluding a gap around 500 nm, which was fitted. Both instruments delivered data with a resolution of 10 min.

2.3 Atmospheric and surface properties - inputs to models

2.3.1 Surface properties

MODIS 6th collection daily product M*D09CMG was used to retrieve surface albedo values over the area between 55ºN and 90ºN with a resolution of 1º x 1º. Data were averaged over 1 month to obtain a good coverage, thus assumed constant and inserted into the Fu-Liou model (Markowicz et al., 2017b).

    Spectral dependency of surface albedo derived from the MODTRAN built-in module, using calculations of the Fresnel

15 reflection at the ocean top, was used while comparing data to Fu-Liou results. Additional set-up of radiometer derived surface albedo was used for the comparison with RF, calculated by means of the radiometer measurements. Both MODTRAN and Fu-Liou codes assumed a flat and horizontal Earth surface.

MODIS MCD43A1 surface product of Bidirectional Reflectance Distribution Function (BRDF) on 12 July 2015 (closest to the simulation day), at 469 nm, was however, used for the 3D Monte Carlo model over the Svalbard area. The BRDF was calculated yielding the equation of Strahler et al. (1999):

$$R(\Theta, \vartheta, \phi, \lambda) = f_{iso}(\lambda) + f_{vol}(\lambda) \cdot K_{vol}(\Theta, \vartheta, \phi) + f_{geo}(\lambda) \cdot K_{geo}(\Theta, \vartheta, \phi) \tag{1}$$

5 where f and K stand for coefficient kernels, in particular: 'iso' denotes isotropic scattering component, 'geo' diffuse reflection component and 'vol' volume scattering component. Θ, ϑ and ϕ are solar zenith angle, view zenith angle and view-sun relative azimuth angle respectively. Gaps over land were filled in with mean values of parameters for a given surface type (glacier or tundra/rock) and elevation range. The coastal line used to distinguish between water and land was taken from the Norwegian Polar Institute (2014a). Glacier outlines (last updated 1st April 2016) were taken from Svalbard land covering map dataset

10 (Norwegian Polar Institute, 2014b). Fresnel reflection from the water surface was assumed in the modeling. Moreover, radiation scattering by seawater and its constituents (e.g. phytoplankton or mineral suspended matter) was neglected.

The digital elevation model (DEM) used in the Monte Carlo modeling was based on maps from Norwegian Polar Institute (2014a) (UTM zone 33N projection, ellipsoid WGS84). The original DEM was generalized to a resolution of 200 m. The land surface altitude within a cell is estimated by the following equation (Ricchiazzi and Gautier, 1998):

15 $$z = a_0 \cdot x + a_1 \cdot y + a_2 \cdot x \cdot y + a_3 \tag{2}$$

where x, y, and z are the coordinates of a given point of a cell surface and a_0, a_1, a_2, and a_3 are coefficients fitted to the coordinates of the cell nodes. The Earth's surface approximated in such a way is continuous.

2.3.2 Vertical profiles of thermodynamic variables and ozone concentration

Profiles of all thermodynamic properties, including pressure (p), temperature, wind speed, and RH were adopted from the

20 radio-soundings performed in Ny-Ålesund for the day of interest. Data above profiles were filled in by subarctic summer profiles from the international standard atmosphere. They were further used for 3D Monte Carlo, MODTRAN and EULAG simulations. The profiles for the Fu-Liou calculations were taken from the Navy Operational Global Analysis and Prediction System (NOGAPS).

Vertical profiles of ozone were retrieved from dimensional climatology, UGAMP (Li and Shine, 1995), then scaled to the

25 measured values of the total ozone content by the MODIS M*D09CMG product (Fu-Liou model), and SP1a photometer (the remaining models).

2.3.3 Vertical profiles of single-scattering properties

Vertical profiles of single-scattering properties at ambient conditions are used as input parameters to MODTRAN and Monte Carlo calculations. The retrieval is based on the in situ single-scattering properties, measured at the surface in dry conditions

(denoted later on as superscript 'd'), and on vertical profiles of σ_{ext}^a, as well as RH at ambient conditions (hereinafter superscript 'a') from KARL lidar and radio-sounding data.

In the reference to temporal variability of range-corrected signal, measured at 532 nm by Micropulse Lidar, Markowicz et al. (2016a), characterize smoke plume as a rather well-mixed layer of BB aerosol extending from around 4 - 6 km on 9th to 0 - 3.5 km later on. Both contributions of BB-like aerosol in the NAAPS AOD, estimated on the level as high as 80%, and the similarity between columnar and in situ aerosol extensive properties such as α (Markowicz et al., 2016a), suggest that smoke plume may have crossed PBL and mixed with the lowermost part of the troposphere. Additionally, very little aerosol load existing above smoke plume plays a minor role in affecting the radiative properties of the atmosphere and therefore may be neglected. This is why, in the presented methodology, we assume no changes in chemical composition vertically, so that most of the possible vertical variability of ω^a at ambient conditions, is attributed to changes in RH. Therefore, we approximate initial profiles of ω^d and R_{eff}^d by setting them up to the values of in situ measurements and consider them constant with altitude. By introducing hygroscopic growth model for particles with known size distribution, one may obtain ω^a profile as well as g^a.

Algorithm for delivering single scattering albedo profile ω at ambient conditions

From absorption (σ_{abs}) and scattering (σ_{scat}) coefficients at 530 nm (for details see Tab. 1), ω can be calculated yielding:

$$\omega(\lambda, z) = 1 - \frac{\sigma_{abs}(\lambda, z)}{\sigma_{ext}(\lambda, z)} \tag{3}$$

at ambient and dry conditions. Subsequently, since σ_{abs} is a weak function of RH (Zieger et al., 2011), the assumption that σ_{abs}^a and σ_{abs}^d are identical is justified. We can then relate dry and ambient conditions, by introducing the scattering enhancement factor $f(\lambda, z(RH))$ principle, being defined as the ratio between scattering coefficients measured at mentioned RH states (Zieger et al., 2010):

$$f(\lambda, z(RH)) = \frac{\sigma_{scat}^a(\lambda, z(RH))}{\sigma_{scat}^d(\lambda, z)} \tag{4}$$

Ultimately, from 3 and 4 formulas, we may introduce the equation for ω^a satisfying:

$$\omega^a(\lambda, z) = \frac{1}{1 + \frac{1 - \omega^d(\lambda, z)}{\omega^d(\lambda, z) \cdot f(\lambda, z(RH))}} \tag{5}$$

Therefore, to derive the relationship between the aerosol water uptake and a particular aerosol species, the Handel model (Hänel, 1976) of growth factor $f(RH)$ is used, relating hygroscopicity of aerosols with relative humidity, yielding:

$$f(RH) = \left(\frac{1 - RH^a}{1 - RH^d}\right)^{-\gamma} \tag{6}$$

where γ parameter represents the indicator of particle hygroscopicity. Larger γ is referred to more hygroscopic aerosols. In this study, a literature value of γ was introduced, equal to 0.18, which applies for biomass burning aerosols (Reid et al., 2005). In this method we combine lidar and in situ measurements, an issue with lack of data exists within the lidar geometrical compression range (0 - 700 m), which is solved by an interpolation method. The proposed method leads to ω^a uncertainty of 0.05, where its vast majority may be attributed to σ_{abs}^d and σ_{scat}^d measurement uncertainties.

Algorithm for delivering asymmetry parameter g at ambient conditions

Asymmetry parameter g is derived iteratively using aerosol size distributions, measured by SMPS and APS, the Mie theory, as well as one-parameter equation determined by Petters and Kreidenweis (2007), that approximates the relation between RH and growth factor $\chi(RH)$, yielding:

$$\chi(RH) = \left(1 + \kappa \frac{RH}{1 - RH}\right)^{\frac{1}{3}} \tag{7}$$

where RH represents the relative humidity, while neglecting the Kelvin effect (in terms of the Köhler law), which is true for particles affecting significantly light extinction (diameter > 0.01 µm; Zieger et al., 2011; Bar-Or et al., 2012). Coefficient κ however, refers to particle hygroscopicity, with respect to the Raoult effect. In this study we neglect the effect of broadening of the aerosol size distribution spectra, due to diffusional growth of particles for simplification purposes. To determine the most accurate literature value of κ coefficient for the BB aerosol, that vastly relies on flora being burnt, we studied the trajectory of smoke transport over the Arctic by the means of GEM-AQ model and analysed a source area (in the event under study - Alaska), regarding vegetation coverage. κ coefficient of 0.07 (0.25 µm dry diameter) was chosen to match vegetation (Duff core) covering the Alaskan tundra (Carrico et al., 2010).

The size distributions of aerosols at ambient conditions were estimated by introducing the hygroscopic growth factor $\chi(RH)$, related to growth of particles due to water uptake, yielding:

$$\chi(RH) = \frac{D^a(RH)}{D_d(RH)} \tag{8}$$

where D is the diameter of the particle at a certain RH (Zieger et al., 2010).

The calculations are provided for an extreme biomass burning event, thus, as previously mentioned, a concentration of aerosols other than smoke is negligible. That is why, for retrieval of g at ambient conditions by the means of the Mie theory, we used a constant refractive index for biomass burning aerosol (1.52 - 0.0061i; Sayer et al., 2014).

2.3.4 Equations governing 3D Monte Carlo simulations

The results from 3D Monte Carlo model, as mentioned earlier, are used to characterise spatial variability of RF and therefore to diagnose possible uncertainties resulting from using single-column radiative transfer models, represented by MODTRAN and Fu-Liou codes. Taking into account the above goals, we resigned from performing time-consuming simulations of daily mean broadband RFs for the model domain; and instead we relied on the relative value of RF calculated for 1 λ, with respect to its value at TOA at a given zenith angle. Such an approach allowed for defining higher spatial resolution.

The relative net irradiance F_{net}^{rel} at the Earth's surface was computed according to the equation:

$$F_{net}^{rel} = \frac{F_{net}}{F_{toa}} = \frac{S_c}{S_s \cdot N_{toa}} \sum_{j=1}^{N} w_j \tag{9}$$

where F_{net} is the net irradiance aligned with the direction of the vector normal to the sloping surface in column (k, l), F_{toa} is the downward irradiance at TOA, N_{toa} is the number of photons incident at TOA(k, l), S_s is the area of the Earth's surface

within the column (k, l), S_c is the area of the cell (k, l), N is the number of photons absorbed by the Earth's surface within the column (k, l), and w_j is the weight of the jth photon absorbed by the Earth's surface within the column (k, l).

The short-wave direct aerosol radiative forcing (spectral relative radiative forcing) , $RF_{rel}(\lambda)$, is expressed as:

$$RF_{rel}(\lambda) = \frac{F_{net}^{aer}(\lambda) - F_{net}^0(\lambda)}{F_{toa}(\lambda)} = F_{net}^{aer,rel}(\lambda) - F_{net}^{0,rel}(\lambda) \tag{10}$$

where superscript 'aer' stands for a clear-sky conditions with an aerosol included and superscript '0' for a clear-sky without one. We can also define RF with respect to the cell surface S_c instead of the actual surface within a given column S_s:

$$RF_{rel}^{cell}(\lambda) = S_s \cdot RF_{rel}(\lambda) \tag{11}$$

3   Results

3.1   The temporal variability of aerosol single-scattering properties during BB event in Ny-Ålesund

In July 2015 a transport of biomass-burning plume over the Arctic region was observed, being advected from the intense tundra and Boreal forest fires in the northern parts of North America. The plume altered both the optical and microphysical properties of aerosols as indicated by the in situ and ground-based remote sensing instruments installed in Ny-Ålesund. Thus, τ conditions characteristic to summer conditions were changed with a magnitude of 10, making it the strongest event in 25 years (Markowicz et al., 2016a). Markowicz et al. (2016a) reported the development and further intensification of tundra fires in Alaska, introduced by a series of frequent lightning strikes occurring from mid-June to late July 2015. The transport of BB plume was visible between 4th and 6th July, from the central part of Alaska, via the North Pole, to the Spitsbergen. Starting in the afternoon of the 9th July, till approximately noon 11th July, the BB plume was visible in Ny-Ålesund as indicated by in situ and remote sensing instruments (Fig. 1). As suggested by lidar data Markowicz et al. (2016a), this advection lasted longer in the area of study, however, the appearance of clouds around noon on the 11th (Fig. 1b) terminated further measurements. Although Markowicz et al. (2016a) reported the beginning of the event at 14:00 UTC, based on the lidar data, we see the temporal discrepancy between in situ and remote sensing measurements of half a day, resulting from a transport taking place in the mid-troposphere (Fig. 1d). The ultimate manifestation of a BB plume at the surface however, might be evidence of a turbulent vertical mixing.

The event was characterized by the mean τ_{550} value estimated at the level of 0.64, with a maximum reaching as high as 1.2 at noon, on 10th July (Fig. 1a). The temporal variability of α was rather stable, with an average value of around 1.5 throughout the advection, which indicates an existence of mostly fine particles. This hypothesis is confirmed by the aerosol size distribution measured at ground level, which shows that particles during the BB event are mainly distributed in the accumulation mode (Moroni et al., 2017).

The mean ω^d at 530 nm obtained for the event is 0.94±0.02 (Fig. 1b), indicating moderate absorbing properties, characteristic for aged BB plumes. Note that the value is slightly higher than in situ ω^d reported by Moroni et al. (2017), of 0.91, resulting from the applied additional multiple-scattering correction to PSAP data in this study. During the most intense period ω^d reduces
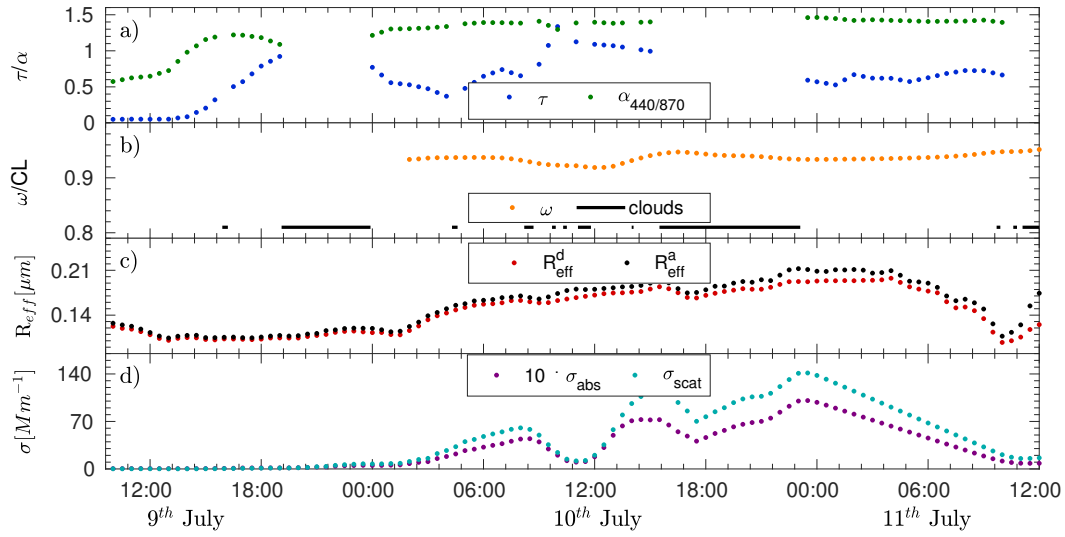
Figure 1. Temporal variability of aerosol single-scattering properties during BB2015 event over Ny-Ålesund, in particular aerosol optical depth τ at 530 nm (blue dots) and Ångstrom exponent α (green dots) measured by SP1a (a), single-scattering albedo ω^d at 530 nm (yellow dots) calculated from in-situ data and cloud coverage CL (black line) from the pyranometer (b), effective radiuses at dry R_{eff}^d (red dots) and ambient R_{eff}^a (black dots) conditions measured by SMPS and APS (c) as well as absorption coefficient σ_{abs} multiplied 10 times (purple dots) and scattering coefficient σ_{scat} (light blue dots) at 530 nm obtained from PSAP and Nephelometer.

to 0.9. Aerosol absorbing properties decrease over the event, resulting in the increase of ω^d on 11th July to its maximum value of 0.95. Lund Myhre et al. (2007) presented results from the transport of smoke-enriched air masses over Ny-Ålesund. The episode was very similar to the one under study, as the mean τ_{440} reached the value of 0.64 with a mean ω of 0.98, after 7 days of transport from Central Europe. It is clearly visible that ω is slightly higher by comparison to BB2015. Apart from the above

5   paper, the representation of BB plumes lasting in the atmosphere for more than 3 days, in literature, is rather seldom. Reid et al. (2005) reported a number of mean surface ω, characterizing aged BB plumes ranging from 0.76 to 0.93, from various in situ measurements. Although values usually seem to be much lower by comparison to the BB2015 event, the differences result from the definition of aged plumes. In the mentioned Reid et al. (2005), aged aerosol was characterized as a plume existing in the atmosphere for more than 24 hours only; while in this study, its persistence is much longer (around 7 days).

10   The mean value (14:00 July 9th - 11:30 July 11th) of absorption coefficient (σ_{abs}) was 4.0 Mm^{-1}, while extinction coefficient (σ_{ext}) was 65.0 Mm^{-1}, as indicated by in situ instruments (Markowicz et al., 2016a) during BB2015. Reported extensive optical properties of aerosols significantly exceeded typical annual mean values of (σ_{scat}: 4.35 Mm^{-1};σ_{abs}: 0.18 Mm^{-1}, α: 1.15), characterized by Schmeisser et al. (2018) for the station at the Zeppelin Mt. (475 m a.s.l.), located close to Ny-Ålesund.

15   We obtained the average values of 0.17 ± 0.02 μm and 0.18 ± 0.02 μm for effective radius at dry (R_{eff}^d) and ambient (R_{eff}^a) conditions respectively (Fig. 1c). Presented results are in good agreement with studies provided by Nikonovas et al. (2015),

who reported the values of R^a_{eff} originating from open shrublands, to be as high as 0.176 - 0.194 µm. R^a_{eff} being in the lower boundary of the class reported by Nikonovas et al. (2015), is likely to result from the chemical composition of the smoke plume, which doesn't allow for intense hygroscopic growth of aerosols (consisting mainly of hydrophobic particles; Moroni et al., 2017). We may also speculate that it is due to the efficiency of scavenging processes with much longer transport.

5 Additionally, Markowicz et al. (2016a) present a significant increase in the precipitable water (PW), of up to 2.2 cm; rather unusual in the High Arctic. The advection of such humid air-masses may significantly enhance the water uptake of aerosols, therefore using in situ measurements (with RH usually of around 15% in the chamber), possibly leads to an appreciable underestimation of aerosol scattering, and thus radiative properties.

3.2 Retrieval of the single-scattering properties at ambient conditions

10 An analysis concerning the identification of a source region was performed by means of the GEM-AQ model. We investigated the path of smoke back-trajectories, while transported across the Arctic region (not shown), and confirmed that the studied BB plume originated from wildfires over Alaska. Both the timing and inflow of aerosol-enriched air masses and the rapid increase of τ_{550} may support the above statement. Vertical profiles of PM_{10} demonstrated polluted air masses extending up to approximately 3 km, with maximum mass mixing ratios reaching 35 ppb at 2 km. Analysis of 3-D extinction fields over 15 Svalbard revealed a thick layer with higher values above the PBL (Fig. 2b$_{1-4}$). The model reproduced the altitude of elevated extinction coefficients, however, the complex vertical stratification was not captured by the model, due to sparse vertical resolution. In this subsection, we present exemplary results of applied methodology concerning the retrieval of ω^a profile. The first case (11:30 10th July; Fig. 2a$_1$-e$_1$), in terms of σ^a_{ext} profiles, represents the moment of maximum τ value, while 2-3 cases indicate average conditions, characterizing BB plume (23:00 10th July; Fig. 2a$_2$-e$_2$; 02:30 11th July; Fig. 2a$_3$-e$_3$). The last 20 chosen case outlines the transition of the atmosphere with intensified atmospheric dynamics, an appreciable turbulent mixing and convective cloud formation, to the conditions where a formation of low clouds relying on stable conditions is visible, and thus, it is likely that vertical mixing is gradually suppressed.

 The vertical profiles of thermodynamic variables, such as RH and potential temperature (θ), were retrieved from two radio-soundings performed on the 10th and 11th July, around noon. θ profile indicates the existence of 2 rather thick inversion 25 layers at around ground level and at 3.5 km, as well as an almost isothermal layer at 2-3.5 km (Fig. 2e$_{1-2}$). The profiles on the next day revealed that all layers were attenuated during the day and were significantly lifted (Fig. 2e$_{3-4}$). The appearance of additional thin inversions, together with a visible decay in θ lapse rate and the mentioned transformations of previous layers, suggest the existence of vertical mixing. Similar vertical structure is visible in RH profiles with values oscillating around 15 - 90%. A significant decay in RH values is attributed to θ inversion layers; in between however, the values usually exceed 75%. 30 The vertical structure of σ^a_{ext} (Fig. 2a$_{1-4}$) retrieved from the lidar observations is strongly dependent on both θ and RH profiles. The latter designates the enhancement of σ^a_{ext} inside the visible layers, attributed to hygroscopic growth of aerosols, while θ determines their thickness. Overall, the smoke plume is visible from around ground level to 3.5 km. However, the shape of the lower boundary is uncertain, due to the lidar overlap issue under 0.7 km. σ^a_{ext} inside the smoke layer ranges from 100 - 350 Mm^{-1}, with a significant vertical variability. In all cases an additional secondary σ^a_{ext} enhanced layer is visible above
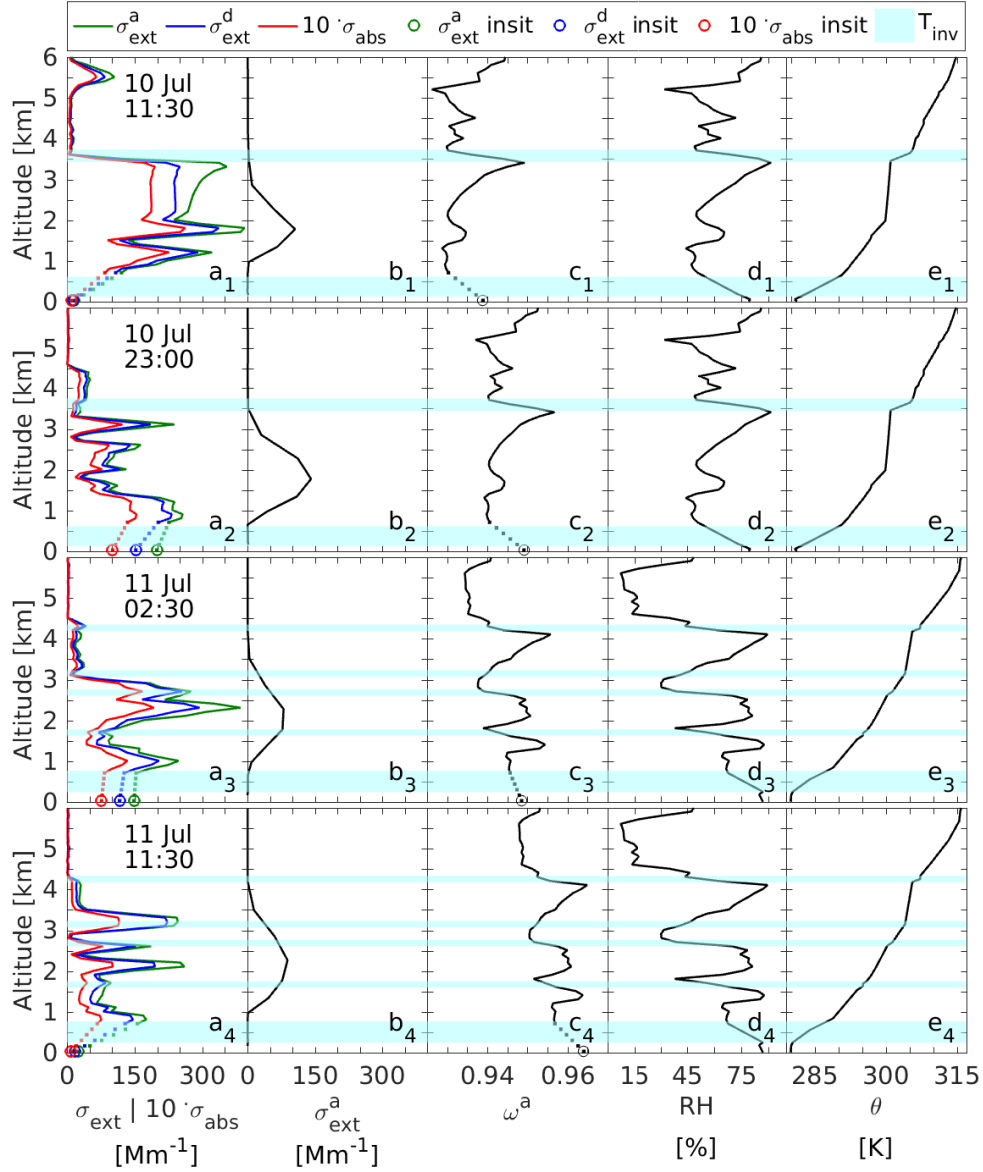
Figure 2. Vertical profiles of aerosol single-scattering properties at 530 nm on 10th and 11th July 2015 (UTC), based on the lidar, radio-sounding profiles and model's output (lines), as well as in-situ measurements (dots). Subfigures include extinction coefficient at ambient (σ_{ext}^{a}; green) and dry (σ_{ext}^{d}; blue) conditions, as well as absorption coefficient σ_{abs} multiplied 10 times (red; a_{1-4}), modeled extinction profile from GEM-AQ (σ_{ext}^{a}; b_{1-4}), retrieved single-scattering albedo ω^{a} (c_{1-4}) at ambient conditions, radio-sounding profiles of relative humidity RH (d_{1-4}), and potential temperature θ (e_{1-4}). Blue transparent layers denote temperature inversions (T_{inv}).

the main BB plume. In the 1 case, it is visible at around 5.5 km, and is likely connected with the existence of thin clouds of marginal meaning in light of the smoke plume itself. In the remaining cases, secondary layers visible at 3.5 - 4.5 km, may be the residuum of cumulus clouds, reported by Markowicz et al. (2016a), resulting from mixing processes between smoke and the above layer of the air mass. In Fig. $2a_{1-4}$ the vertical variability of retrieved σ_{ext}^d and σ_{abs} are additionally presented. σ_{ext}^d represents the result of Eq. 3-6, where the hygroscopic growth of aerosol is removed. The calculated profiles of ω^a vary from 0.93 to 0.96. In the presented cases, ω^a profiles shift towards less absorbing properties. The vertical structure of ω^a strongly mitigates the shape of the RH profiles as a result of applied approximations (in particular Eq. 6).

3.3 Comparison of model-derived irradiances with the measurements

Figure 3 presents the results of the performance of MODTRAN simulations compared with in situ measurements, in terms of radiative properties of the atmosphere. The Pearson correlation coefficients for MOTRAN and radiometer data exceed 0.95 for all radiation components (in particular total incoming (F_{in}) - 0.95, outgoing (F_{out}) - 0.99, direct (F_{dir}) - 0.99, diffuse (F_{diff}) - 0.98 fluxes at the surface), suggesting well-defined statistical dependence of the variables. Nevertheless, the model seems to slightly underestimate all fluxes with regards to measurement data, especially visible in F_{diff}. Root mean square error (RMSE) is estimated on the level of 18.5 Wm^{-2} and 7.6 Wm^{-2} regarding F_{in} and F_{out}. The mean bias of total incoming flux at the surface is mainly related to RMSE of F_{diff}, that is as high as 13.1 Wm^{-2}. The F_{dir} RMSE is almost 2 times lower than the latter and reaches 7.0 Wm^{-2}. This difference in biases of F_{dir} and F_{diff} result from the distinction in parameters governing both irradiances, in particular F_{dir} is a function of parameters that are measured with good accuracy (τ and PW), while F_{diff} is additionally controlled by variables with appreciably higher uncertainty (ω, phase function, surface albedo etc.).

Although, cloud-contaminated radiometer data was previously removed, higher RMSEs together with relatively high temporal variability of F_{diff}, which is a significant function of cloud coverage, might suggest that the performance of cloud-screening algorithm was insufficient for the case under study. Therefore, presented results from in situ data should be used with caution, bearing in mind that they may periodically represent all-sky conditions.
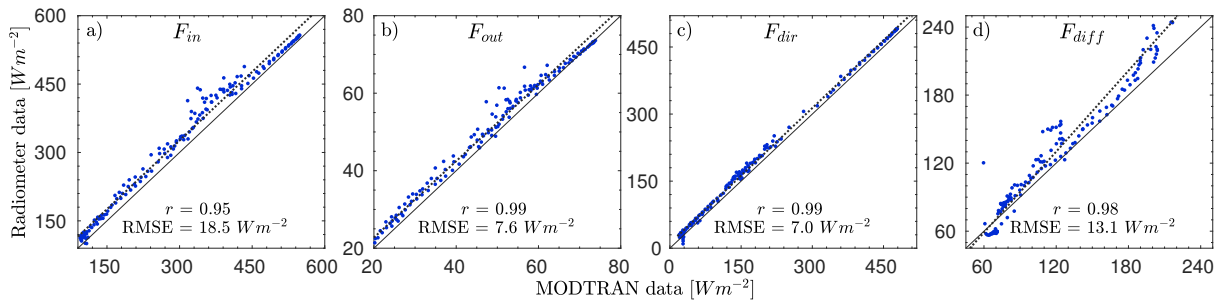
Figure 3. The comparison of model-derived and measured irradiances, in particular: incoming F_{in} (a), outgoing F_{out} (b), direct F_{dir} (b) and diffuse F_{diff} (c) surface fluxes on 9th - 11th July 2015. Solid black line refers to the perfect and dotted black line to a linear fit.

3.4 Temporal variability of radiative forcing in Ny-Ålesund

Results presented in this chapter were previously introduced in the section 2.3.3 concerning ω^a and g^a retrieval. To estimate the overall performance of the mentioned approximation we performed 2 initial simulations, that assumed fixed values of all optical and microphysical properties of aerosol except for ω and g. In the first one, we utilized ω^d and g^d measured by in situ instruments, while the second one applied ω^a and g^a approximations. Differences between the two simulations indicated the decrease of RF (in magnitude), on average by about 3.1 Wm^{-2} for the BB event (14:00 July 9th - 11:30 July 11th), when ambient conditions were used. It was due to an increase in both F_{in} and F_{out} by 3.5 Wm^{-2} and 0.4 Wm^{-2} respectively, for simulation with aerosol included. The impact of the retrieval on enhancement of F_{in} and F_{out} might be vastly attributed to ω translation, with the influence of 81% and only 19 % to g^a approximation.

Figure 4 presents the comparison of temporal variability of irradiances (Fig. 4a) and clear-sky RF (Fig. 4b), obtained by means of MODTRAN simulations and estimated jointly by the radiometer measurements in Ny-Ålesund (polluted simulation, see section 2.1) and RTM model calculations (reference simulation, see section 2.1) for the BB2015 event. The daily variability of incoming irradiance at the surface, calculated in the reference simulation (F_{cin}), is mainly the function of solar zenith angle and for the 9th - 11th July 2015, ranges from around 153.0 Wm^{-2} at midnight, to 560.8 Wm^{-2} at noontime. On the other hand, F_{in} is additionally strongly affected by the optical and physical properties of the advected smoke. The model's performance at background conditions might be validated at the period between 7:00 to 14:00 UTC on 9th July. It represents the clear-sky period with an infinitesimal load of aerosols, typical for summer background conditions in the Arctic. Both measured by radiometer (later on as Rad) and modeled by MODTRAN (hereinafter referred to as Mod) F_{in} are in rather good agreement deviating on average, only by 9.7 Wm^{-2} (2 %) from each other and additionally by 0.4 % (Rad F_{in}), as well as 2.3 % (Mod F_{in}) from the reference simulation F_{cin} at the respective background summer conditions. Measured and modelled F_{out} indicate a very good agreement of less than 1 %, both reaching on average 69.8 Wm^{-2} (Rad) and 69.4 Wm^{-2} (Mod), respectively.

At 14:00 UTC Markowicz et al. (2016a) reported an advection of BB plume over Ny-Ålesund, characterized by a complicated structure of the BB layers, with a mixture of aerosol and clouds. Since the mean value of Mod F_{in} during the event (14:00 9th - 11:30 11th July) is estimated on the level of 243.0 Wm^{-2}, the existence of the BB aerosol reduced the incoming flux, on average, by around 90 Wm^{-2} when compared to the case represented by summer background conditions (332.1 Wm^{-2}; 7:00 to 14:00 UTC on 9th July). Furthermore, we report the mean value of outgoing irradiance (Mod F_{out}), reaching 36.9 Wm^{-2}. The highest decrease in Mod F_{in} is visible on 10th July, where reduction exceeded 30 % in comparison with daily Mod F_{cin}, and was as high as 27 % regarding the summer background conditions (compare 7:00 - 14:00 UTC on 9th and 10th July). This is believed to be indicated by the observed maximum of τ_{550}. We may expect that higher variability of Rad F_{in}, visible by comparison to the 9th July, together with an appearance of clouds inside the smoke plume, are likely to result from both a possible BB aerosol activation and increased turbulence. Further to this, a number of high- and mid-level cumulus clouds are reported around noon and in the afternoon (Markowicz et al., 2016a).

We report the average radiative forcing at the surface (RF_{surf}) of the studied smoke plume (14:00 July 9th - 11:30 July 11th) on the level of -78.9 Wm^{-2} (Mod) and -43.3 Wm^{-2} (Rad), indicating a significant cooling effect of BB aerosol at the surface.
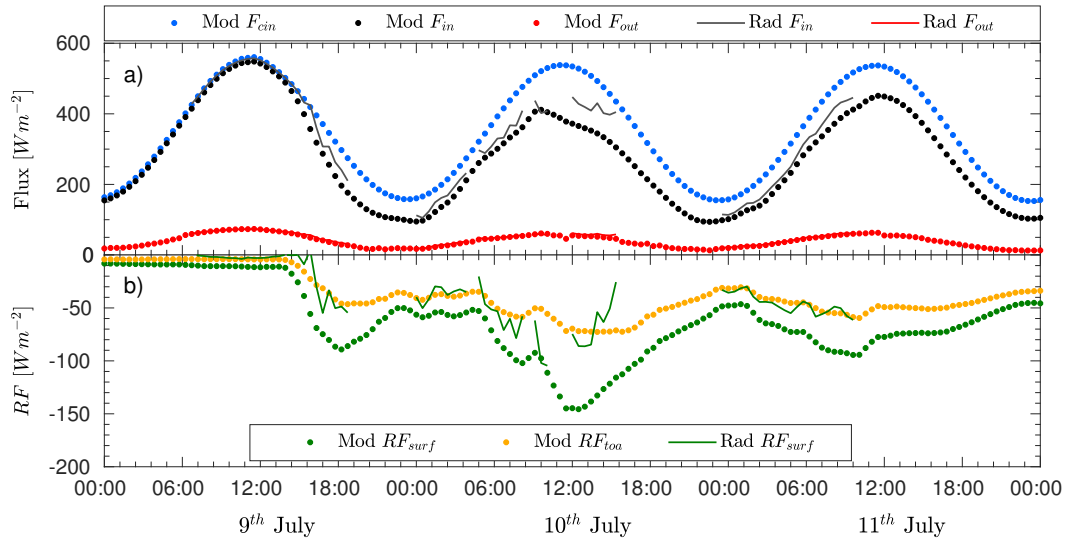
Figure 4. Temporal variability of (a) the surface radiation fluxes: total incoming flux with the presence of aerosols F_{in} (black) and without aerosol load F_{cin} (blue), as well as total outgoing flux F_{out} (red), simulated by MODTAN (dots) and measured by radiometers (lines). The gaps in the radiometer data refer to the cloud contamination. Sub-figure (b) presents radiative forcing at the surface RF_{surf} (green) and at the top of atmosphere RF_{toa} (orange).

Radiometer data represent all-sky conditions, since the discussed BB event is extremely complicated and therefore a possible cloud contamination seems to be impossible to separate entirely. However, periods with a clear influence of clouds were removed (i.e. 15:00-21:00 10th July), therefore the presented mean value of RF, lacks the most intense period (see Fig. 4b). The highest values (in magnitude) are observed at around 12:00 UTC on 10th July, being attributed to, as previously mentioned

5 in this chapter, the highest values of τ_{550}. Thus, a momentary Mod RF_{surf} exceeded -147 Wm^{-2} regarding MODTRAN simulations. Similar results were reported by Stone et al. (2008), who studied smoke advected from Alaska to the Canadian Arctic during 2nd July 2004. Authors came to conclusions that an average diurnal τ_{500}, of 0.5 would produce a cooling effect at the surface, reaching 40 Wm^{-2}. Since in our case the average τ_{550} is 0.64, the results seem to be complementary. On the other hand, a study from Sitnov et al. (2013) reveals smaller absolute values of RF_{surf} at much higher τ_{550} for the wildfires

10 observed in the European Russia at the beginning of August 2010. For the average τ_{550} being between 0.98 - 1.16, authors estimated RF_{surf} to be around -60 Wm^{-2}. As RF_{surf} is a function of solar zenith angle (Stone et al., 2008), the duration of the positive solar zenith angle and surface albedo (Carslaw et al., 2010), the discrepancies between both variables might be the explanation of the reported differences.

The average value of Mod RF_{toa} exceeded -47 Wm^{-2}, indicating BB plume to cool the entire atmospheric column. Within

15 the atmosphere, it has however, a positive impact of 31.9 Wm^{-2} (Mod RF_{atm}). This pattern is in agreement with Stone et al. (2008) who also reported negative values at TOA and positive ones when an atmospheric layer is considered. High single-scattering albedo values and negative RF_{toa} clearly show that scattering is dominant with respect to the light absorption

contribution. Indeed, absorption species (mainly BC) are able to mitigate the cooling effect of the BB event in the atmosphere, but not sufficient to change the RF sign. This means that BC particles play a minor role with respect to scattering particles (sulfate, organic carbon (OC), etc.). That could also be demonstrated by the changes in atmospheric concentrations of BC, OC, and sulfate measured at Gruvebadet. In particular, the relative concentrations increase about 20 times for BC and OC, and

5   about 10 times for non-sea-salt sulfate during the BB event, with respect to the background level. In spite of the BC and OC, relative increases are similar; the absolute concentrations of OC are more than 10 times higher than atmospheric concentration of BC (Moroni et al., 2017). Overall, the described RF of the plume had about 31 % higher (in magnitude) influence at the surface, in comparison with TOA. Model calculations usually overestimate Mod RF_{surf} values, which on an average deviate from Rad RF_{surf} of around 32.9%, possibly related to all-sky conditions being represented by Radiometer measurements, that

10   increase diffusive flux.

The mean estimated radiative forcing efficiency at the surface (Mod RFE_{surf}) of the BB event in Svalbard of -126 $\mathrm{Wm}^{-2}/\tau_{550}$, is slightly higher by comparison to other estimates of smoke transport, like -99 $\mathrm{Wm}^{-2}/\tau_{550}$ reported by Markowicz et al. (2016b) for the Canadian forest fires advection over Europe in 2013, and -88 $\mathrm{Wm}^{-2}/\tau_{550}$ for wildfires observed over Crete, Greece in 2001 (Markowicz et al., 2002). On the other hand, multiyear mean RFE_{surf} values obtained for different

15   regions are appreciably higher, i.e. RFE_{surf} originating from tropical forest wildfires over the Amazon basin, is estimated on the level of -140 ± 33 $\mathrm{Wm}^{-2}/\tau_{550}$; while Boreal forest fires from North America are as high as -173 ± 60 $\mathrm{Wm}^{-2}/\tau_{550}$ and RFE_{surf} for African Savannas, are at the level of -183 ± 31 $\mathrm{Wm}^{-2}/\tau_{550}$ (García et al., 2012). We found that the reported discrepancies are a function of both solar zenith angle, surface albedo, and single-scattering properties of aerosols. In general, more efficient $RFEs_{surf}$ are characterized by smoke plumes with lower values of ω i.e. 0.85 and 0.91 for African Savannas

20   and the Amazon forest, respectively (García et al., 2012). Although ω values are similar for the case under study and i.e. Boreal forest, the latter is more efficient due to a higher solar zenith angle.

3.5   The comparison of RF derived from MODTRAN and Fu-Liou simulations

This chapter focuses on the comparison of RFs simulated by MODTRAN and Fu-Liou models. The results of the latter were previously published in Markowicz et al. (2017b) regarding BB transport over the Northern Hemisphere. In the following

25   subsection, all RFs were retrieved over the ocean area near Ny-Ålesund (78.5°N, 9.5°E), assuming a spectral surface albedo of the Fresnel reflection over a water body.

Table 2 presents the comparison between input variables to both models: mean daily ω^a, PW, and τ_{550}. Column-integrated Mod ω^a is calculated yielding (Schafer et al., 2014):

$$\omega^a = \frac{\int\limits_{0}^{10km} \sigma_{ext}^a(z) \cdot \omega^a(z) dz}{\tau} \tag{12}$$

30   while ω^a in case of MODTRAN simulations has an increasing trend (from 0.92 to 0.96) within 9 - 11th July, the same quantity show more absorbing properties by 3 - 6 %, and is rather constant for Fu-Liou calculations oscillating around 0.91 - 0.93. The same trend is visible for PW mean values, where it is between 1.72 - 2.26 cm for MODTRAN simulations, however, for

Table 2. The mean daily values of the single-scattering albedo ω^a, precipitable water PW [cm], and aerosol optical depth τ_{550} at 550 nm used as inputs to MODTRAN and Fu-Liou simulations.

| | ω^a | | | PW [cm] | | | τ_{550} | | |
	9th	10th	11th	9th	10th	11th	9th	10th	11th
Modtran	0.92	0.94	0.96	1.72	2.26	2.22	0.23	0.72	0.55
FuLiou	0.93	0.91	0.92	0.98	2.08	1.98	0.20	0.54	0.59

Fu-Liou it is by 10 - 40 % lower. Additionally, retrieved mean MODTRAN τ_{550} equal to 0.23 - 0.72 and Fu-Liou value of 0.2 - 0.59, seem to deviate from each other by 8 - 35 %. What is more, while the highest τ_{550} value for MODTRAN simulations is on 10th July, for the Fu-Liou, it is noticeable on 11th July. Presented discrepancies between variables are satisfactory, given the fact that Fu-Liou model has larger spatial resolution.
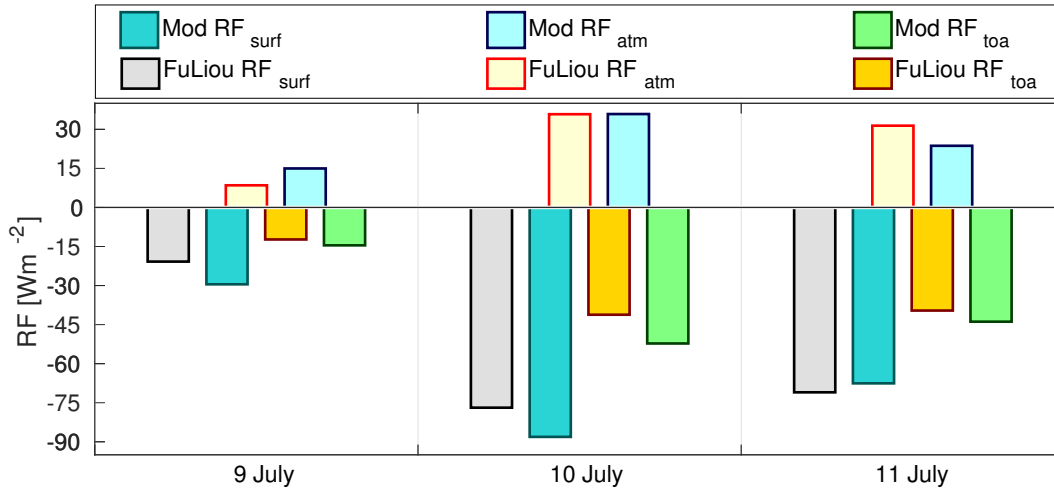
Figure 5. The mean daily values of radiative forcing (RF) calculated by means of Fu-Liou (FuLiou) and MODTRAN (Mod) models. Simulations were run for clear-sky conditions at the surface (subscript 'surf'), within the atmosphere (subscript 'atm'), and at the top of the atmosphere (subscript 'toa'). The surface reflectance in MODTRAN simulations is based on the Fresnel reflection calculations at the ocean surface.

5   Figure 5 presents the daily mean values of RFs derived from MODTRAN and Fu-Liou calculations for BB2015 event at the surface, within the atmosphere (RF_{atm}), as well as at TOA for clear-sky conditions. Overall, the difference between daily mean values of MODTRAN and Fu-Liou simulations is, on average, close to around 15 %, with all assumed input variables and calculated RFs being lower for the latter (with the exception of RF_{atm}). Differences between MODTRAN and Fu-Liou simulations are vastly connected with slightly different aerosol optical properties. Since for each model, different resolution of
10 input parameters over the slightly distinct area were used, authors consider obtained accuracy to be fairly good.

Given the fact that RF_{toa} for all-sky conditions modeled by Fu-Liou is equal to -14.0 Wm^{-2} (not shown) on 10th July, these results are considered exceptional in the Arctic records and are of a similar magnitude as other investigations on aerosol high load events in this region. All-sky RF_{toa} for BB transport from Europe in 2006, was estimated between -12 and 0 Wm^{-2} (Lund Myhre et al., 2007).

3.6 3D distribution of radiative forcing at the surface in the vicinity of Kongsfjorden

In the previous sections, we discussed the RF computed for a single cell. In the described approach, both topographic effects (shading, slope inclination, etc.) and small (subgrid) scale variability in surface albedo were neglected. In this section however, the above effects are taken into consideration and are analysed in light of RF variability, and thus, uncertainty resulting from single-cell radiative transfer schemes in the vicinity of Konsfjorden.

The simulations were performed for a single wavelength λ=469 nm and the solar position for the time of the retrieval of aerosol properties' profile (10th July 2015 11:30 UTC; solar zenith angle=57°, solar azimuth=173°). Moreover, photon transfer between atmospheric columns was assumed zero. RF was also computed using the plane-parallel geometry for individual 200 m cells/columns (ICA - Independent Column Approximation). In this method the Earth's surface is assumed flat (horizontal) and uniform within each column. Moreover, the horizontal photon exchange between column boundaries is neglected; thereby neither optical properties of the surface and atmosphere, nor topography of adjacent cells, influence surface radiative forcing in this atmospheric ICA column. Shading, slope inclination, and strong horizontal photon transport neglected in this method, lead to biased local estimates of radiative forcing.

In this section, RF is expressed as a fraction of downward irradiance at TOA (Eq. 9-11). Further in this section, we will skip λ and RF_{rel}, RF_{rel}^{cell} and RF_{rel}^{pp} will denote relative spectral RF, simulated using the 3D modeling, $RF_{rel}(\lambda$=469 nm), $RF_{rel}^{cell}(\lambda$=469 nm), and the plane-parallel approach to individual cells, $RF_{rel}^{pp}(\lambda$=469 nm).

Figure 6 shows the spatial distribution of RF_{rel} (Eq. 10) at the surface and compares it to the distribution derived using the ICA approach. The mean values of RF and the standard deviations are compared in Table 3. In the analysed case, the domain mean values and standard deviation of RF_{rel} is -0.1817 ± 0.1066 for the RF calculated with respect to the real inclined surface (i.e. per unit area of the inclined surface; compare Eq. 9-10), and RF_{rel}^{cell} is -0.1875 ± 0.1104 when the RF is calculated with respect to the horizontal cell surface (i.e. per unit area of the cell surface; compare Eq. 11). There is a large difference between the RF over water and land surfaces, which is mainly due to differences in surface albedo between these regions. For the fjord surface, an absolute value of RF is smaller and weakly variable over the fjord surface, mean RF_{rel}^{cell} is equal to mean RF_{rel} and reaches -0.2632 ± 0.0092. Its coefficient of variation is 3.5%. The actual value of RF variability over the sea may be even lower, because the noise of Monte Carlo method may enhance it. The land RF is characterized with both RF_{rel}^{cell} and RF_{rel} less negative mean values of -0.1395 ± 0.1180, as well as -0.1326 ± 0.1084 respectively, and much stronger surface variability. The respective coefficients of variation are 84.6% and 81.7%. In our simulation, the variability of RF over the sea is caused by an impact of the surrounding land only. Apart from shading the sky and the sun by the orography, the spatial variability of RF and its deviations from the plane-parallel RF values, are caused by positive net horizontal photon transfer from the land area. Horizontal photon transfer due to reflection between the atmosphere and the underlying surface is efficient over bright

-0.64 -0.56 -0.48 -0.40 -0.32 -0.24 -0.16 -0.08 0.00 0.08 0.16
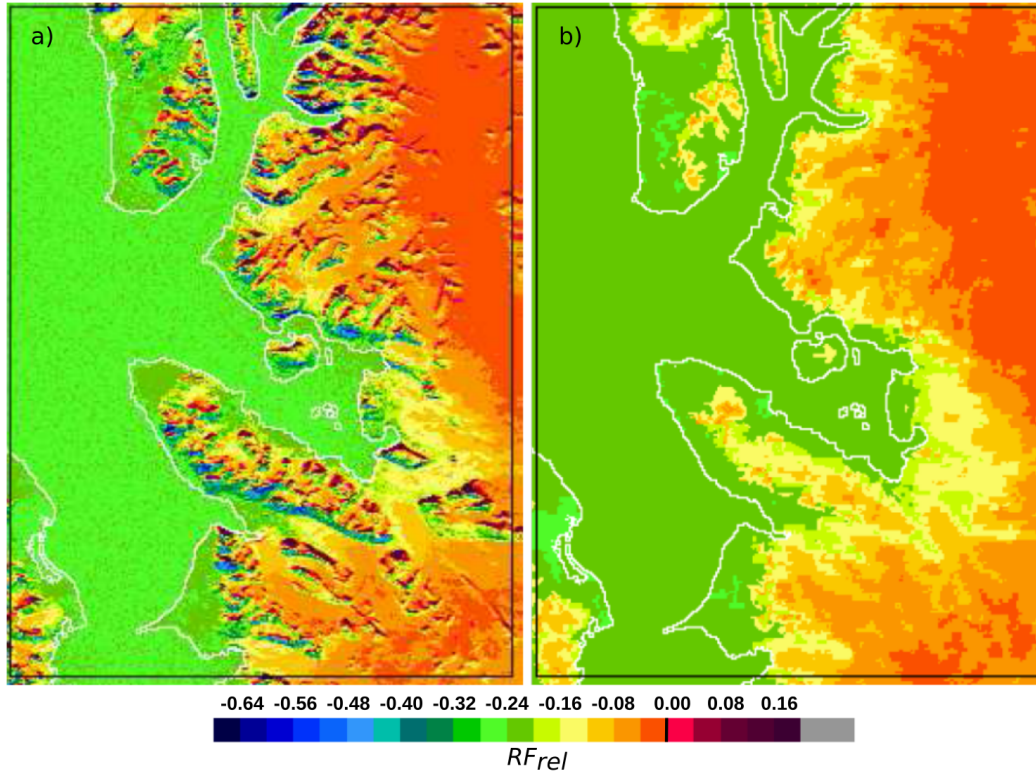
RF_rel

Figure 6. A comparison of the RF_{rel} distribution at the Earth's surface derived from 3D Monte Carlo model (a) with RF_{rel}^{pp} distribution (b) computed, applying the Monte Carlo model with plane-parallel geometry to each pixel independently (ICA). In (b) both the surface topography and photon exchange between adjacent columns are neglected. Computations for λ=469 nm, solar zenith angle=57°, solar azimuth=173°, and aerosol properties of 10th July 2015, 11:30 UTC.

areas, such as snow-covered land and glaciers. The horizontal distance of the photon transmission outside the bright underlying surface, relates to the effective height at which the radiation reflected upward by the Earth's surface, is reflected downward by the atmosphere. The net horizontal transport is observed for both atmospheres, with and without aerosols, but in each case the effective height of reflection is different. An appearance of dense, low-lying aerosol layer reduces the effective reflection height
5   and thus, the horizontal distance the photons can travel over the fjord; but at the same time, it intensifies the reflectance of the atmosphere, compared to the case without aerosols. Thus the gradient in irradiance, with distance from the reflective land is stronger in the aerosol case. The atmosphere without aerosols acts similarly to a very thin cloud located higher over the Earth's surface, while aerosol layer can be compared to a thicker cloud with its base at a lower height (Rozwadowska and Górecka, 2012).
10   The main factors influencing RF and its variability over land in the vicinity of Ny-Ålesund comprise of reflective properties of the land surface, slope exposition concerning the sun, and shading of the sun by the mountains. The impact of photons

reflected from nearby sunlit slopes and horizontal photon transport due to multiple reflections between the sky and the surface on RF variability, are of secondary importance over the land.

In the analysed case, the highest magnitude of negative RF was found for sun-facing slopes of white sky albedo of around 0.2. In such places, the effective solar zenith angle is relatively low and a high contribution of the direct solar radiation to the total irradiance results in a substantial reduction in the surface irradiance due to the presence of aerosols, hence, an RF_{rel} of about -0.39. In the main, for slopes lit by diffused radiation, the RF is positive, i.e. presence of aerosols increases the amount of radiation absorbed by the surface. In shaded places with the effective solar zenith angle of approximately 90° and white sky albedo of around 0.4, RF_{rel} can be as high as 0.07 in our simulation. Using the ICA approach to RF estimation results

Table 3. Mean relative radiative forcing RF calculated concerning the actual surface, RF_{rel}, and the horizontal cell surface RF_{rel}^{cell} using the 3D Monte Carlo model. RF_{rel}^{pp} is RF computed, using the Independent Column Approximation approach. Computations were done for λ=469 nm, solar zenith angle=57°, solar azimuth=173°, and aerosol properties of the 191st day of 2015.

	All cells	Water	Land
RF_{rel}	-0.1817 ± 0.1066	-0.2632 ± 0.0092	-0.1326 ± 0.1084
RF_{rel}^{cell}	-0.1875 ± 0.1104	-0.2632 ± 0.0092	-0.1395 ± 0.1180
RF_{rel}^{pp}	-0.1842 ± 0.0824	-0.2586 ± 0.0000	-0.1372 ± 0.0734
RF_{rel}^{cell}-RF_{rel}^{pp}	-0.0032 ± 0.0699	-0.0047 ± 0.0092	-0.0024 ± 0.0890

in an underestimation of the surface variability in the RF, also results in biased domain mean values of the RF. In the case under study, the mean difference between the more accurate RF for the horizontal cell surface and the RF calculated using the plane-parallel approach, RF_{rel}^{cell} and RF_{rel}^{pp} are -0.0032 ± 0.0699, which is 1.9 % of the mean RF_{rel}^{cell}. This, in conversion to daily mean shortwave RF, gives the average error not exceeding 2 Wm^{-2} while using the plane-parallel approach. Thus, it is almost as high as the effect of ω^d translation to ambient conditions considered in our study. Additionally, the mean bias is higher for the sea than for the land. However, for individual cells/columns, the variability of deviations from the real value of RF_{rel}^{cell} is much larger for the land, where the standard deviation of the difference RF_{rel}^{cell}-RF_{rel}^{pp} equals 63.8% of the mean RF_{rel}^{cell}. The negative bias with the largest magnitude of 0.247 was found for the case of sun-facing slopes discussed above. For shaded inclined areas, the plane-parallel approach seriously underestimates radiative forcing where the mean bias equals 0.233.

3.7 Impact of biomass burning aerosol on the atmospheric dynamics

ILESs (see section 2.1) performed using the EULAG model indicates an appreciable impact of the BB plume on atmospheric dynamics. Figure 7 presents the development of potential temperature and turbulent kinetic energy (TKE) in a reference simulation (Fig. 7b,c) representing a clear atmosphere, as well as in a polluted simulation (Fig. 7e,f), including effects related to the BB plume. Initial profiles used in the simulations are based on the radio-sounding from 10th July 12:00 UTC and the

applied heating rates given, by:

$$r_h = \frac{1}{\rho \cdot C} \frac{\partial F_{net}}{\partial z} \tag{13}$$

whereby ρ is air density and C is a specific heat capacity defined both for short- and longwave, irradiances are obtained from
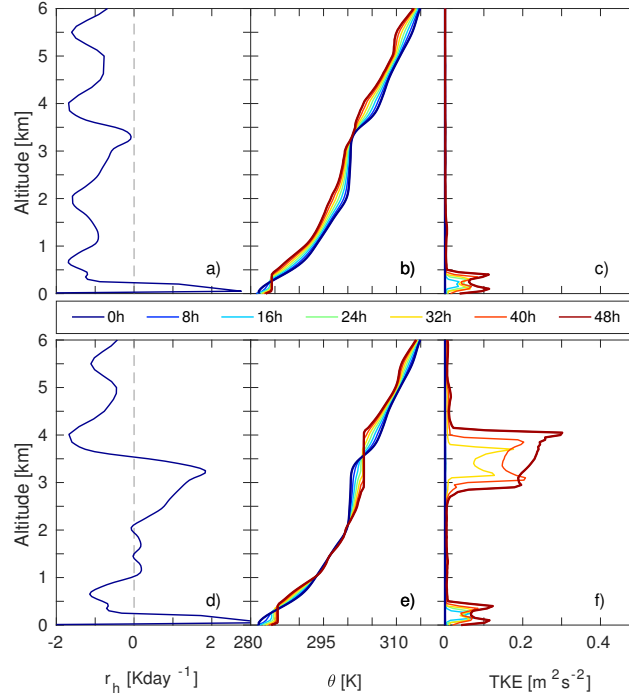
Figure 7. Vertical profiles of applied heating rate r_h (a,d), and horizontally averaged potential temperature θ (b,e), and turbulent kinetic energy TKE (c,f) for simulations of a reference case (a-c) and a polluted case with effects of aerosol load included (d-f). Simulation data is stored at 8 h intervals.

MODTRAN simulations for 10th July 11:30 UTC. The r_h profiles for the reference case (Fig. 7a) and the aerosol polluted case (Fig. 7d) both show a thin layer near the surface (z<0.5 km) with significant heating: 2.7 and 3.4 Kday^{-1} respectively. Above 0.5 km, the reference case indicates the cooling of the atmosphere at a rate of approximately 1 Kday^{-1}, while in the polluted case, another layer with significant heating effects is visible between altitudes of 1 and 3.5 km. The heating rate in the lower part of this layer is around 0.2 Kday^{-1}, while in the upper part it reaches values of up to 1.8 Kday^{-1}. The two simulations have the same initial profile of θ which is represented by the navy blue lines in Figure 7b,e. There is a layer between altitudes of 2 and 3 km with nearly constant initial θ, but in general, it decreases with altitude. Due to the stable initial stratification and the lack of, e.g. strong surface heating, turbulence develops slowly in the performed simulations (see TKE profiles in Fig. 7c,f). After 16 h, a turbulent layer starts to develop near the surface in both simulations. The TKE in this layer reaches values of around 0.1 m^{2}s^{-2} and it extends up to 0.5 km at the time t=48 h. After 24 h, a second turbulent layer starts to develop in the polluted case, at an altitude of approximately 3.4 km. The thickness of this layer increases with time, and at t=48 h,

it covers altitudes between 2.5 and 4.2 km with maximum TKE values of 0.3 $m^2 s^{-2}$ and updrafts/downdrafts with vertical velocities of around 1 ms^{-1}. By contrast, the flow in the reference case remains almost non-turbulent above 0.5 km, with vertical velocities close to zero throughout the simulation period. In the regions with relatively high TKE, θ becomes nearly constant with altitude, and the polluted simulation indicates that the initially well-mixed layer around z=2.5 km expands and moves upwards over time.

Outside the clearly turbulent regions very little vertical mixing takes place, and the potential temperature is approximately given by:

$$\theta = \theta(0, z) + r_h \cdot t \qquad (14)$$

where 'z' symbolises altitude and 't' time.

4   Conclusions

This paper presented the investigation of a strong biomass-burning plume advection that was observed during 9th-11th July 2015 over the Arctic. In this research study, we focused on the local perturbations in the radiation budget as well as atmospheric dynamics concerning the Ny-Ålesund area on Spitsbergen. The discussed biomass-burning aerosol advection was one of the most spectacular regarding the last 25 years (Lund Myhre et al., 2007), with all aerosol optical properties typical for the summer conditions enhanced by the factor of more than 10. In particular, mean daily values of aerosol optical depth at 550 nm, precipitable water and single-scattering albedo exceeded 0.2-0.7, 1.7-2.2 cm, as well as 0.93-0.97 respectively, according to in situ and photometer data at Ny-Ålesund. Here, we want to underline the most significant outcome from our investigation:

– Simulations with the GEM-AQ model confirmed the source region (Alaskan tundra) and the arrival time at Ny-Ålesund of the biomass-burning plume, indicating a reasonable agreement in the extinction profile when compared to lidar measurements. The apparent underestimation of aerosol loading in the plume may be connected to rather coarse horizontal and vertical resolutions. Also, a large distance from the source region (approximately 4000 km) may have enhanced the uncertainties of the model output.

– Retrieved effective radius from in situ measurements of around 0.18 ±0.02 μm, mean value of single-scattering albedo of 0.96, as well as an average asymmetry parameter exceeding 0.62 (all at ambient conditions), suggest moderate absorbing properties of the plume. Presented properties are in agreement with the results performed by Nikonovas et al. (2015), who characterized a various set of smoke optical and microphysical properties retrieved from AERONET stations. Taking into account that BB2015 variables are rather placed in the lower part of the statistics in Nikonovas et al. (2015), we may conclude that during this prolonged transport, scavenging processes were more efficient.

– Lidar profiles indicate the existence of biomass-burning plume at the level of 0 - 3.5 km with a complicated structure of sublayers limited by a number of (2- 5) temperature inversions. A complex vertical variability is also visible in the

relative humidity profile. The retrieved ω^a profiles vary from 0.92 to 0.97, enhancing with time. The highest values are associated with the bottom part of temperature inversions.

- The accuracy of modeled irradiances during the summer background conditions, represented by 9:00 - 14:00 9th July, is considered sufficient deviation from the measured quantities by 2 % and 1 %, regarding F_{in} and F_{out} respectively. During the biomass-burning event (14:00 July 9th - 11:30 July 11th) the differences increase to 10 % and 5.8 % on average.

- We report mean values of modeled RF_{surf}, RF_{atm}, and RF_{toa} for the biomass-burning episode under study (14:00 July 9th - 11:30 July 11th) at the level of -78.9 Wm^{-2}, -47.0 Wm^{-2}, and 31.9 Wm^{-2}. The values indicate cooling effects at the surface and TOA while RF_{atm} reveals relatively strong heating within the atmosphere. It might be translated into up to 2 Kday^{-1} of the heating rate inside the smoke plume (0 - 3.5 km). Obtained values are consistent with results reported for the similar period, and likely the same solar zenith angles performed by Stone et al. (2008).

- An averaged RFE_{surf} at the smoke event is as high as -125.9 $\mathrm{Wm}^{-2}/\tau_{550}$, indicating higher values in comparison with $RFEs_{surf}$ obtained for wildfires from boreal regions (Markowicz et al., 2002, 2016b); while for other fire sources it is considerably lower by 12 - 32 % (García et al., 2012). Authors believe the main reason among different aerosol intensive properties, is distinct solar zenith angle and high value of daily mean solar radiation at TOA during the Arctic summer.

- The discrepancies between modelled RFs obtained for MODTRAN and fast Fu-Liou simulations, oscillate around 15 %, with lower values usually attributed to the latter (exception for the atmospheric values). Considering different inputs and spatial resolution used for both simulations, the results are satisfactory.

- The mean bias of RFs associated with single-cell RF simulations in the vicinity of Kongsfjorden, is estimated by 3D Monte Carlo model on the level of 2 Wm^{-2}.

- ILES indicates that the main impact of the BB plume on the atmospheric dynamics is a graduate vertical expansion and positive displacement of the BB layer characterized by neutral stratification. The turbulent kinetic energy in the simulated BB layer is around 0.3 $\mathrm{m}^2\mathrm{s}^{-2}$. In a reference simulation without effects from the BB plume included, the flow remained nearly non-turbulent throughout the simulation period.

In this study we have shown that long-range transport of wildfire aerosols from Alaska to European Arctic, certainly has a significant impact on radiative properties. Furthermore, our results also indicate an impact on atmospheric dynamics. We believe that the detailed studies on this topic are needed, especially considering a significant positive trend in mid-latitudes fire frequency during the summer season in the last 25 years; and therefore possibly more frequent advection over the Arctic region (Young et al., 2017).

Competing interests. The authors declare no conflict of interests.

Acknowledgements. The authors would like to acknowledge the support of this research from the Polish-Norwegian Research Programme, operated by the National Centre for Research and Development under the Norwegian Financial Mechanism 2009-2014, within the frame of Project Contract No Pol-Nor/196911/38/2013.

The authors are grateful for support from Marion Matturilli for providing data from the Baseline Surface Radiation Network (BSRN),
5 measured at AWIPEV station in Ny-Ålesund.

The EULAG simulations were performed at the Interdisciplinary Centre for Mathematical and Computational Modeling (ICM), University of Warsaw, under grant number G64–5.

References

Alexandrov, M. D., Marshak, A., Cairns, B., Lacis, A. A., and Carlson, B. E.: Automated cloud screening algorithm for MFRSR data, Geophysical Research Letters, 31, 524–543, 2004.

Aubé, M. P., O'Neill, N., and Royer, A.: Modelling of aerosol optical depth variability at regional scale, in: Geoscience and Remote Sensing Symposium, 2000. Proceedings. IGARSS 2000. IEEE 2000 International, vol. 1, pp. 199–201, IEEE, 2000.

Aubé, M. P., O'Neill, N. T., Royer, A., and Lavoue, D.: A modeling approach for aerosol optical depth analysis during forest fire events, Proc.SPIE, 5548, 5548–5558, 2004.

Bar-Or, R., Koren, I., Altaratz, O., and Fredj, E.: Radiative properties of humidified aerosols in cloudy environment, Atmospheric Research, 118, 280 – 294, 2012.

Berk, A., Bernstein, L., Anderson, G., Acharya, P., Robertson, D., Chetwynd, J., and Adler-Golden, S.: MODTRAN Cloud and Multiple Scattering Upgrades with Application to AVIRIS, Remote Sensing of Environment, 65, 367 – 375, 1998.

Bernstein, L., Berk, A., Robertson, D., Acharya, P., Anderson, G., and Chetwynd, J.: Addition of a Correlated-k Capability to MODTRAN, Proc. IRIS Targets, Backgrounds and Discrimination, 2, 239–248, 1996.

Bond, T. C., Doherty, S. J., Fahey, D. W., Forster, P. M., Berntsen, T., DeAngelo, B. J., Flanner, M. G., Ghan, S., Kärcher, B., Koch, D., Kinne, S., et al.: Bounding the role of black carbon in the climate system: A scientific assessment, Journal of Geophysical Research: Atmospheres, 118, 5380–5552, 2013.

Carrico, C. M., Petters, M. D., Kreidenweis, S. M., Sullivan, A. P., McMeeking, G. R., Levin, E. J. T., Engling, G., Malm, W. C., and Collett Jr., J. L.: Water uptake and chemical composition of fresh aerosols generated in open burning of biomass, Atmospheric Chemistry and Physics, 10, 5165–5178, 2010.

Carslaw, K. S., Boucher, O., Spracklen, D. V., Mann, G. W., Rae, J. G. L., Woodward, S., and Kulmala, M.: A review of natural aerosol interactions and feedbacks within the Earth system, Atmospheric Chemistry and Physics, 10, 1701–1737, 2010.

Côté, J., Gravel, S., Méthot, A., Patoine, A., Roch, M., and Staniforth, A.: The Operational CMC–MRB Global Environmental Multiscale (GEM) Model. Part I: Design Considerations and Formulation, Monthly Weather Review, 126, 1373–1395, 1998.

Dubovik, O., Smirnov, A., Holben, B. N., King, M. D., Kaufman, Y. J., Eck, T. F., and Slutsker, I.: Accuracy assessments of aerosol optical properties retrieved from Aerosol Robotic Network (AERONET) Sun and sky radiance measurements, Journal of Geophysical Research: Atmospheres, 105, 9791–9806, 2000.

Dubovik, O., Holben, B., Eck, T. F., Smirnov, A., Kaufman, Y. J., King, M. D., Tanré, D., and Slutsker, I.: Variability of Absorption and Optical Properties of Key Aerosol Types Observed in Worldwide Locations, Journal of the Atmospheric Sciences, 59, 590–608, 2002.

Fu, Q. and Liou, K. N.: On the Correlated k-Distribution Method for Radiative Transfer in Nonhomogeneous Atmospheres, Journal of the Atmospheric Sciences, 49, 2139–2156, 1992.

Fu, Q. and Liou, K. N.: Parameterization of the Radiative Properties of Cirrus Clouds, Journal of the Atmospheric Sciences, 50, 2008–2025, 1993.

García, O. E., Díaz, J. P., Expósito, F. J., Díaz, A. M., Dubovik, O., Derimian, Y., Dubuisson, P., and Roger, J.-C.: Shortwave radiative forcing and efficiency of key aerosol types using AERONET data, Atmospheric Chemistry and Physics, 12, 5129–5145, 2012.

Gong, S. L.: A parameterization of sea-salt aerosol source function for sub- and super-micron particles, Global Biogeochemical Cycles, 17, 1097, 1097, 2003.

Gras, J. L., Jensen, J. B., Okada, K., Ikegami, M., Zaizen, Y., and Makino, Y.: Some optical properties of smoke aerosol in Indonesia and tropical Australia, Geophysical Research Letters, 26, 1393–1396, 1999.

Grinstein, F. F., Margolin, L. G., and Rider, W. J.: Implicit large eddy simulation: computing turbulent fluid dynamics, Cambridge university press, 2007.

5 Hansen, J., Bond, T., Cairns, B., Gaeggler, H., Liepert, B., Novakov, T., and Schichtel, B.: Carbonaceous aerosols in the industrial era, Eos, Transactions American Geophysical Union, 85, 241–244, 2004.

Haywood, J. and Osborne, S.: Corrections to be applied to the PSAP and nephelometer for accurate determination of the absorption coefficient, scattering coefficient and single scattering albedo, MRF Tech. Note, 31, 2000.

Henyey, L. G. and Greenstein, J. L.: Diffuse radiation in the galaxy, The Astrophysical Journal, 93, 70–83, 1941.

10 Herber, A., Thomason, L. W., Gernandt, H., Leiterer, U., Nagel, D., Schulz, K.-H., Kaptur, J., Albrecht, T., and Notholt, J.: Continuous day and night aerosol optical depth observations in the Arctic between 1991 and 1999, Journal of Geophysical Research: Atmospheres, 107, 2002.

Hoffmann, A.: Comparative aerosol studies based on multi-wavelength Raman LIDAR at Ny-Ålesund, Spitsbergen, PhD Thesis Uni. Potsdam, 2011.

15 Hänel, G.: The Properties of Atmospheric Aerosol Particles as Functions of the Relative Humidity at Thermodynamic Equilibrium with the Surrounding Moist Air, vol. 19 of *Advances in Geophysics*, Elsevier, 1976.

IPCC: Climate Change 2001: The Scientific Basis. Contribution of Working Group I to the Third Assessment Report of the Intergovernmental Panel on Climate Change, [Houghton, J.T., Ding, Y., Griggs, D. J., Noguer, M., van der Linden, P.J., Dai, X., Maskell, K., Johnson, C.A. (eds.)], pp. 1–1144, Cambridge University Press, 2001.

20 Janicka, L., Stachlewska, I. S., Veselovskii, I., and Baars, H.: Temporal variations in optical and microphysical properties of mineral dust and biomass burning aerosol derived from daytime Raman lidar observations over Warsaw, Poland, Atmospheric Environment, 169, 162–174, 2017.

Kaiser, J., Heil, A., Andreae, M., Benedetti, A., Chubarova, N., Jones, L., Morcrette, J.-J., Razinger, M., Schultz, M., Suttie, M., et al.: Biomass burning emissions estimated with a global fire assimilation system based on observed fire radiative power, Biogeosciences, 9, 25 527, 2012.

Kaminski, J., Neary, L., Struzewska, J., McConnell, J., Lupu, A., Jarosz, J., Toyota, K., Gong, S., Côté, J., Liu, X., et al.: GEM-AQ, an on-line global multiscale chemical weather modelling system: model description and evaluation of gas phase chemistry processes., Atmospheric Chemistry and Physics, 8, 3255–3281, 2008.

Koch, D., Schulz, M., Kinne, S., McNaughton, C., Spackman, J., Balkanski, Y., Bauer, S., Berntsen, T., Bond, T. C., Boucher, O., et al.: 30 Evaluation of black carbon estimations in global aerosol models, Atmospheric Chemistry and Physics, 9, 9001–9026, 2009.

Kotchenruther, R. A. and Hobbs, P. V.: Humidification factors of aerosols from biomass burning in Brazil, Journal of Geophysical Research: Atmospheres, 103, 32 081–32 089, 1998.

Kreidenweis, S. M., Remer, L. A., Bruintjes, R., and Dubovik, O.: Smoke aerosol from biomass burning in Mexico: Hygroscopic smoke optical model, Journal of Geophysical Research: Atmospheres, 106, 4831–4844, 2001.

35 Li, D. and Shine, K. P.: A 4-dimensional ozone climatology for UGAMP models, UGAMP Internal Rep, 35, 1995.

Lund Myhre, C., Toledano, C., Myhre, G., Stebel, K., Yttri, K., Aaltonen, V., Johnsrud, M., Frioud, M., Cachorro, V., Frutos, A. d., et al.: Regional aerosol optical properties and radiative impact of the extreme smoke event in the European Arctic in spring 2006, Atmospheric Chemistry and Physics, 7, 5899–5915, 2007.

Lynch, P., Reid, J. S., Westphal, D. L., Hogan, T. F., Hyer, E. J., Curtis, C. A., Hegg, D. A., Campbell, J. R., Rubin, J. I., Sessions, W. R., Turk, F. J., et al.: An 11-year global gridded aerosol optical thickness reanalysis (v1. 0) for atmospheric and climate sciences, Geoscientific Model Development, 9, 1489–1522, 2016.

Magi, B. I., Hobbs, P. V., Schmid, B., and Redemann, J.: Vertical profiles of light scattering, light absorption, and single scattering albedo during the dry, biomass burning season in southern Africa and comparisons of in situ and remote sensing measurements of aerosol optical depths, Journal of Geophysical Research: Atmospheres, 108, 2003.

Marchuk, G. I., Mikhailov, G. A., Nazareliev, M., Darbinjan, R. A., Kargin, B. A., and Elepov, B. S.: The Monte Carlo methods in atmospheric optics, vol. 12, Springer, 2013.

Markowicz, K., Pakszys, P., Ritter, C., Zielinski, T., Udisti, R., Cappelletti, D., Mazzola, M., Shiobara, M., Xian, P., Zawadzka, O., et al.: Impact of North American intense fires on aerosol optical properties measured over the European Arctic in July 2015, Journal of Geophysical Research: Atmospheres, 121, 14 487–14 512, 2016a.

Markowicz, K. M., Flatau, P. J., Ramana, M., Crutzen, P., and Ramanathan, V.: Absorbing Mediterranean aerosols lead to a large reduction in the solar radiation at the surface, Geophysical Research Letters, 29, 1968, 2002.

Markowicz, K. M., Chilinski, M., Lisok, J., Zawadzka, O., Stachlewska, I., Janicka, L., Rozwadowska, A., Makuch, P., Pakszys, P., Zielinski, T., et al.: Study of aerosol optical properties during long-range transport of biomass burning from Canada to Central Europe in July 2013, Journal of Aerosol Science, 101, 156–173, 2016b.

Markowicz, K. M., Ritter, C., Lisok, J., Makuch, P., Stachlewska, I., Cappelletti, D., Mazzola, M., and Chilinski, M.: Vertical variability of aerosol single-scattering albedo and equivalent black carbon concentration based on in-situ and remote sensing techniques during the iAREA campaigns in Ny-Ålesund, Atmospheric Environment, 164, 431–447, 2017a.

Markowicz, K. M., Lisok, J., and Xian, P.: Simulations of the effect of intensive biomass burning in July 2015 on Arctic radiative budget, Atmospheric Environment, 171, 248 – 260, 2017b.

Marshak, A., Davis, A., Wiscombe, W., and Titov, G.: The verisimilitude of the independent pixel approximation used in cloud remote sensing, Remote sensing of environment, 52, 71–78, 1995.

Maturilli, M., Herber, A., and König-Langlo, G.: Surface radiation climatology for Ny-Ålesund, Svalbard (78.9 N), basic observations for trend detection, Theoretical and Applied Climatology, 120, 331–339, 2015.

Moroni, B., Cappelletti, D., Crocchianti, S., Becagli, S., Caiazzo, L., Traversi, R., Udisti, R., Mazzola, M., Markowicz, K., Ritter, C., et al.: Morphochemical characteristics and mixing state of long range transported wildfire particles at Ny-Ålesund (Svalbard Islands), Atmospheric Environment, 156, 135–145, 2017.

Mtetwa, L. and McCormick, M. P.: Development of Biomass Burning Gaseous and Particulate Emissions Database for Assimilation Into Air Quality Forecast Systems., AGU Fall Meeting Abstracts, 2003.

Müller, T., Nowak, A., Wiedensohler, A., Sheridan, P., Laborde, M., Covert, D. S., Marinoni, A., Imre, K., Henzing, B., Roger, J.-C., et al.: Angular illumination and truncation of three different integrating nephelometers: Implications for empirical, size-based corrections, Aerosol Science and Technology, 43, 581–586, 2009.

Myhre, G., Samset, B., Schulz, M., Balkanski, Y., Bauer, S., Berntsen, T., Bian, H., Bellouin, N., Chin, M., Diehl, T., et al.: Radiative forcing of the direct aerosol effect from AeroCom Phase II simulations, Atmospheric Chemistry and Physics, 13, 1853, 2013a.

Myhre, G., Shindell, D., Bréon, F.-M., Collins, W., Fuglestvedt, J., Huang, J., Koch, D., Lamarque, J.-F., Lee, D., Mendoza, B., et al.: Anthropogenic and Natural Radiative Forcing in Climate Change 2013: The Physical Science Basis. Contribution of Working Group I

to the Fifth Assessment Report of the Intergovernmental Panel on Climate Change, [Stocker, T. F., Qin, D., Plattner, G.-K., Tignor, M., Allen, S. K., Boschung, J., Nauels, A., Xia, Y., Bex, V., Midgley, P. M. (eds.)], p. 659–740, Cambridge University Press, 2013b.

Nikonovas, T., North, P., and Doerr, S. H.: Smoke aerosol properties and ageing effects for northern temperate and boreal regions derived from AERONET source and age attribution, Atmospheric Chemistry and Physics, 15, 7929–7943, 2015.

5   Norwegian Polar Institute: Terrengmodell Svalbard (S0 Terrengmodell), https://doi.org/10.21334/npolar.2014.dce53a47, 2014a.

Norwegian Polar Institute: Kartdata Svalbard 1:100 000 (S100 Kartdata) / Map Data, https://doi.org/10.21334/npolar.2014.645336c7, 2014b.

Orr, C., Hurd, F. K., and Corbett, W. J.: Aerosol size and relative humidity, Journal of Colloid Science, 13, 472–482, 1958.

Ortiz-Amezcua, P., Guerrero-Rascado, J. L., Granados-Muñoz, M. J., Benavent-Oltra, J. A., Böckmann, C., Samaras, S., Stachlewska, I. S., Janicka, Ł., Baars, H., Bohlmann, S., et al.: Microphysical characterization of long-range transported biomass burning particles from

10   North America at three EARLINET stations, Atmospheric Chemistry and Physics, 17, 5931–5946, 2017.

Petters, M. and Kreidenweis, S.: A single parameter representation of hygroscopic growth and cloud condensation nucleus activity, Atmospheric Chemistry and Physics, 7, 1961–1971, 2007.

Prusa, J. M., Smolarkiewicz, P. K., and Wyszogrodzki, A. A.: EULAG, a computational model for multiscale flows, Computers & Fluids, 37, 1193–1207, 2008.

15   Reid, J. S., Eck, T. F., Christopher, S. A., Koppmann, R., Dubovik, O., Eleuterio, D., Holben, B. N., Reid, E. A., and Zhang, J.: A review of biomass burning emissions part III: intensive optical properties of biomass burning particles, Atmospheric Chemistry and Physics, 5, 827–849, 2005.

Ricchiazzi, P. and Gautier, C.: Investigation of the effect of surface heterogeneity and topography on the radiation environment of Palmer Station, Antarctica, with a hybrid 3-D radiative transfer model, Journal of Geophysical Research: Atmospheres, 103, 6161–6176, 1998.

20   Ritter, C., Neuber, R., Schulz, A., Markowicz, K., Stachlewska, I., Lisok, J., Makuch, P., Pakszys, P., Markuszewski, P., Rozwadowska, A., et al.: 2014 iAREA campaign on aerosol in Spitsbergen–Part 2: Optical properties from Raman-lidar and in-situ observations at Ny-Ålesund, Atmospheric Environment, 141, 1–19, 2016.

Rothman, L. S., Rinsland, C., Goldman, A., Massie, S., Edwards, D., Flaud, J., Perrin, A., Camy-Peyret, C., Dana, V., Mandin, J.-Y., et al.: The HITRAN molecular spectroscopic database and HAWKS (HITRAN Atmospheric Workstation): 1996 edition, Journal of quantitative

25   spectroscopy and radiative transfer, 60, 665–710, 1998.

Rozwadowska, A. and Górecka, I.: The impact of a non-uniform land surface on the radiation environment over an Arctic fjord–a study with a 3D radiative transfer model for stratus clouds over the Hornsund fjord Spitsbergen, Oceanologia, 54, 509–544, 2012.

Rozwadowska, A. and Górecka, I.: Impact of reflecting land surface on radiation environment over Hornsund, Spitsbergen–a model study for cloudless skies, Polish Polar Research, 38, 149–174, 2017.

30   Sand, M., Samset, B. H., Balkanski, Y., Bauer, S., Bellouin, N., Berntsen, T. K., Bian, H., Chin, M., Diehl, T., Easter, R., et al.: Aerosols at the poles: an AeroCom Phase II multi-model evaluation, Atmospheric Chemistry and Physics, 17, 12 197–12 218, 2017.

Sayer, A., Hsu, N., Eck, T., Smirnov, A., and Holben, B.: AERONET-based models of smoke-dominated aerosol near source regions and transported over oceans, and implications for satellite retrievals of aerosol optical depth, Atmospheric Chemistry and Physics, 14, 11 493–11 523, 2014.

35   Schafer, J., Eck, T., Holben, B., Thornhill, K., Anderson, B., Sinyuk, A., Giles, D., Winstead, E., Ziemba, L., Beyersdorf, A., et al.: Intercomparison of aerosol single-scattering albedo derived from AERONET surface radiometers and LARGE in situ aircraft profiles during the 2011 DRAGON-MD and DISCOVER-AQ experiments, Journal of Geophysical Research: Atmospheres, 119, 7439–7452, 2014.

Schmeisser, L., Backman, J., Ogren, J. A., Andrews, E., Asmi, E., Starkweather, S., Uttal, T., Fiebig, M., Sharma, S., Eleftheriadis, K., et al.: Seasonality of aerosol optical properties in the Arctic, Atmospheric Chemistry and Physics Discussions, pp. 1–41, https://doi.org/10.5194/acp-2017-1117, 2018.

Screen, J. A. and Simmonds, I.: The central role of diminishing sea ice in recent Arctic temperature amplification, Nature, 464, 1334–1337, 2010.

Sitnov, S., Gorchakov, G., Sviridenkov, M., Gorchakova, I., Karpov, A., and Kolesnikova, A.: Aerospace monitoring of smoke aerosol over the European part of Russia in the period of massive forest and peatbog fires in July–August of 2010, Atmospheric and Oceanic Optics, 26, 265–280, 2013.

Smirnov, A., Holben, B., Eck, T., Dubovik, O., and Slutsker, I.: Cloud-screening and quality control algorithms for the AERONET database, Remote Sensing of Environment, 73, 337–349, 2000.

Smolarkiewicz, P. K.: Multidimensional positive definite advection transport algorithm: an overview, International Journal for Numerical Methods in Fluids, 50, 1123–1144, 2006.

Stamnes, K., Tsay, S.-C., Wiscombe, W., and Jayaweera, K.: Numerically stable algorithm for discrete-ordinate-method radiative transfer in multiple scattering and emitting layered media, Applied optics, 27, 2502–2509, 1988.

Stone, R., Anderson, G., Shettle, E., Andrews, E., Loukachine, K., Dutton, E., Schaaf, C., and Roman, M.: Radiative impact of boreal smoke in the Arctic: Observed and modeled, Journal of Geophysical Research: Atmospheres, 113, 1–17, 2008.

Strahler, A. H., Muller, J., Lucht, W., Schaaf, C., Tsang, T., Gao, F., Li, X., Lewis, P., and Barnsley, M. J.: MODIS BRDF/albedo product: algorithm theoretical basis document version 5.0, MODIS documentation, 23, 42–47, 1999.

Van der Werf, G. R., Randerson, J. T., Giglio, L., Collatz, G., Mu, M., Kasibhatla, P. S., Morton, D. C., DeFries, R., Jin, Y. v., and van Leeuwen, T. T.: Global fire emissions and the contribution of deforestation, savanna, forest, agricultural, and peat fires (1997–2009), Atmospheric Chemistry and Physics, 10, 11 707–11 735, 2010.

Wang, G., Kawamura, K., Watanabe, T., Lee, S., Ho, K., and Cao, J.: High loadings and source strengths of organic aerosols in China, Geophysical research letters, 33, L22 801, 2006.

Wang, H., Rasch, P. J., Easter, R. C., Singh, B., Zhang, R., Ma, P., Qian, Y., Ghan, S. J., and Beagley, N.: Using an explicit emission tagging method in global modeling of source-receptor relationships for black carbon in the Arctic: Variations, sources, and transport pathways, Journal of Geophysical Research: Atmospheres, 119, 12,888–12,909, 2014.

Young, A. M., Higuera, P. E., Duffy, P. A., and Hu, F. S.: Climatic thresholds shape northern high-latitude fire regimes and imply vulnerability to future climate change, Ecography, 40, 606–617, 2017.

Zieger, P., Fierz-Schmidhauser, R., Gysel, M., Ström, J., Henne, S., Yttri, K. E., Baltensperger, U., and Weingartner, E.: Effects of relative humidity on aerosol light scattering in the Arctic, Atmospheric Chemistry and Physics, 10, 3875–3890, 2010.

Zieger, P., Weingartner, E., Henzing, J., Moerman, M., Leeuw, G. d., Mikkilä, J., Ehn, M., Petäjä, T., Clémer, K., Roozendael, M. v., et al.: Comparison of ambient aerosol extinction coefficients obtained from in-situ, MAX-DOAS and LIDAR measurements at Cabauw, Atmospheric chemistry and physics, 11, 2603–2624, 2011.